Development of Early-stage Malaria Treatment and Diagnosis by Hybrid Drugs & Electrical Impedance Spectroscopy

ハイブリッド薬剤と電気インピーダンス分光法による早期マラリア治療薬と診断法の開発

FEBRUARY 2025

MILKA WAMBUI WAITHERA

Graduate School of Science and Engineering

CHIBA UNIVERSITY

(千葉大学審査学位論文)

Development of Early-stage Malaria Treatment and Diagnosis by Hybrid Drugs & Electrical Impedance Spectroscopy

ハイブリッド薬剤と電気インピーダンス分光法による早期マラリア治療薬と診断法の開発

FEBRUARY 2025

MILKA WAMBUI WAITHERA

Graduate School of Science and Engineering

CHIBA UNIVERSITY

Abstract

This thesis aims to develop early-stage malaria treatment and diagnosis by hybrid drugs & electrical impedance spectroscopy (EIS). This study has three originalities 1) the development of hybrid drugs: artesunate 4-Chlorophenoxy aniline (ATSA), 2) the evaluation of artemether-resistance and survival rate, and 3) the quantification of *Plasmodium falciparum* infected RBCs by EIS-distribution of relaxation times (DRT).

The first step is the evaluation of the antimalarial activity of artesunate 4 Chlorophenoxy) aniline (ATSA) *in vitro* and *in vivo* and the prediction of its absorption, distribution, metabolism, and excretion (ADMET) profiles in silico. The reference drug is artesunate (ATS) a derivative of artemisinin recommended by the World Health Organization (WHO) for treating uncomplicated malaria infections in combination with amodiaquine in Southeast Asian malaria-endemic countries. The inhibitory concentration-50 (IC_{50}) for ATSA is 11.47±1.3 ng/ml, 3D7 strain. ATSA has a wide safety margin and a selective index (SI) of 2180.91. The *in vivo* antimalarial chemosuppression is above 40% with effective dosage-50 (ED_{50}: 50% effective inhibitory dosages for *P. berghei* parasites) of 4.211 and 2.601 mg/kg body weight against *P. berghei* ANKA (sensitive strain) and *P. berghei* lumefantrine resistant (LuR) parasites respectively. ATSA exhibited a high predicted human intestinal absorption (HIA) value of > 95% and a medium human ether-a-go-go-related gene (hERG) K^+ channel inhibition risk.

The second step is evaluating artemether resistance and survival rate using mice. Artemether (AM) is a derivative of artemisinin recommended by the WHO for treating uncomplicated malaria infections in combination with lumefantrine mostly in sub-Saharan Africa malaria-endemic countries. The parasites were exposed to increasing dosage of AM and the artemether-resistant parasites' survival rate (AM^R) relative to the sensitive strain (AM^S) in the absence of the drug was determined. Artemether resistance is moderately stable (I_{90} = 15.27, 10.79, and 12.29), and the survival rate is 65.59%.

The third step is the quantification of *Plasmodium falciparum* infected red blood cells (iRBCs) obtained from *in vitro* cultures by EIS-DRT. The electrical impedance was

measured using a conventional impedance analyzer; Hioki IM 7581 by injecting 0.1mA current at a frequency between 0.1-100 MHz. Volume fractions (Ψ) of nucleated chicken nRBCs in un-nucleated porcine uRBCs were used for comparison analysis. A Lab-on-CD (compact disc) prototype device was used to validate the results of iRBCs by measuring the impedance at 10-100 kHz. The results show that the cells' impedance spectra have three DRT peaks: I, II, and III. Peak III with a relaxation frequency of 1.6×10^7 Hz represents the impedance changes in the RBCs' cytoplasm due to biochemical modifications caused by *P. falciparum* invasion or the presence of the nucleus and was selected for further analysis. The amplitude maxima (γ_{max}) of uninfected RBCs was 12.1±0.5 Ω, while the γ_{max} for *P.falciparum* iRBCs decreased from 11.7±0.5 Ω to 9.9±0.5 Ω with the rise in parasitemia from 4.47% to 10.84%. The impedance characteristics from the Lab-on-CD device show consistency with the results obtained from the Hioki IM 7581 where the impedance (Z), phase angle (θ), and real component of complex impedance (Z') decrease gradually with the increase in parasitemia (P); P = 1.55% > P = 2.55%. The technique is envisioned as providing a rapid label-free platform for improved malaria diagnosis or alternative reliable antimalarial drug screening protocol.

Table of Contents

CHAPTER 1

Introduction

1. Introduction

1.1 Early-stage Malaria Treatment

1.1.1 Malaria Treatment

Artemisinin-based combination therapies (ACTs) are the recommended front-line drugs by the World Health Organization (WHO) for treating complicated *Plasmodium falciparum* malaria. ACTs include; artemether-lumefantrine, dihydroartemisinin-piperaquine, artesunate-amodiaquine, and artesunate-pyronaridine [1]. Artemisinin and its derivatives; artemether, artesunate, and dihydroartemisinin are potent antimalarials that rapidly clear the rings and mature trophozoite forms of the parasite; a critical aspect of maintaining their efficacy [2] whereas the long-acting partner drugs eliminate the remaining parasites [3]. The efficacy and continuous use of ACTs are threatened by multidrug-resistant malaria parasites which could render this treatment regimen useless [4]. The search for alternative antimalarials has prompted new research on hybrid drugs which are synthesized by linking two or more compounds with separate individual mechanisms of action into a single molecule, a concept known as molecular hybridization [5].

1.1.2 Artemether Resistance

Monitoring the emergence and spread of drug-resistance genes in the ACTs is a top priority in malaria control and elimination strategies in all malaria-endemic countries [6]. Artemether resistance has recently been reported in Eritrea, Uganda, and Rwanda. Therefore, evaluating artemether resistance and survival rate is crucial as a strategic approach to monitoring the speed of resistance development. Evaluation of drug resistance *in vitro* using the human plasmodium species is difficult to establish. To overcome this setback, mice models have successfully been used to evaluate drug resistance over a short period (a few months) and determine the survival rate, and mutant genes associated with the resistant phenotypes since they are easy to handle [7].

1.2 Early-stage Malaria Diagnosis

Light microscopy is the gold-standard malaria diagnostic tool that identifies parasite species and stages and quantifies parasitemia even though parasite detection depends on Giemsa-stained thick or thin peripheral blood smears, high technical expertise is required for accurate detection of parasites and the procedure is time-consuming [8]. Electrical

impedance spectroscopy (EIS) is a label-free technique widely used in the biomedical field [9]. Previous research has demonstrated the potential of EIS to detect *P. falciparum* parasites even though the measured impedance data is mostly fitted in a complex equivalent circuit model (ECM) to obtain the polarization processes within the system, which requires a priori information [10]. The distribution of relaxation times (DRT) analysis has emerged as an alternative to the ECM for impedance data analysis due to its high temporal resolution. The results are easily interpreted since they are displayed in the time domain as peaks with distinct relaxation time constants associated with separate polarization processes [11].

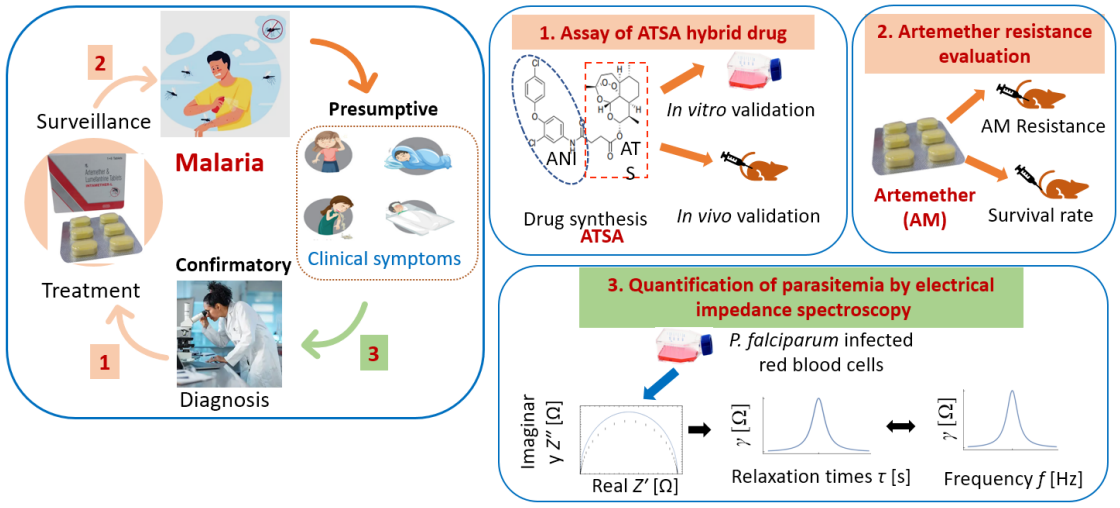

Fig.1. Concept of early-stage malaria treatment and diagnosis by hybrid drugs and electrical impedance spectroscopy.

1.3 Thesis objectives

To address the previously mentioned issues, the author proposed the development of early-stage malaria treatment and diagnosis by hybrid drugs & electrical impedance spectroscopy (EIS). The specific thesis objectives are described below,

1. Development of hybrid drugs: Artesunate 4-Chlorophenoxy Aniline (ATSA)
2. Evaluation of artemether resistance and survival rate
3. Quantification of parasitemia of *Plasmodium falciparum* infected red blood cells by electrical impedance spectroscopy (EIS).

References

[1] P. R. Dimbu *et al.*, “Therapeutic response to four artemisinin-based combination therapies in Angola, 2021,” *Antimicrob Agents Chemother*, vol. 68, no. 4, Apr. 2024.

[2] C. J. Woodrow and N. J. White, “The clinical impact of artemisinin resistance in Southeast Asia and the potential for future spread,” Jan. 01, 2017, *Oxford University Press*.

[3] H. N. Lyu *et al.*, “Study towards improving artemisinin-based combination therapies,” Jul. 01, 2021, *Royal Society of Chemistry*.

[4] M. Dhorda *et al.*, “Artemisinin-resistant malaria in Africa demands urgent action,” *Science*, vol. 385, no. 6706, pp. 252–254, Jul. 2024.

[5] L. S. Feng *et al.*, “Hybrid molecules with potential in vitro antiplasmodial and in vivo antimalarial activity against drug-resistant Plasmodium falciparum,” May 01, 2020, *John Wiley and Sons Inc.*

[6] D. Ménard and A. Mayor, “Knowing the enemy: genetics to track antimalarial resistance,” Dec. 01, 2020, *Lancet Publishing Group*.

[7] J. M.-R. Carlton, K. Hayton, P. V. L. Cravo, and D. Walliker, “Of mice and malaria mutants: unravelling the genetics of drug resistance using rodent malaria models,” 2001. [Online]. Available: http://parasites.trends.com1471

[8] O. O. Oyegoke *et al.*, “Malaria diagnostic methods with the elimination goal in view,” Jul. 01, 2022, *Springer Science and Business Media Deutschland GmbH*.

[9] H. S. Magar, R. Y. A. Hassan, and A. Mulchandani, “Electrochemical impedance spectroscopy (Eis): Principles, construction, and biosensing applications,” Oct. 01, 2021, *MDPI*.

[10] C. Ribaut *et al.*, “Electrochemical impedance spectroscopy to study physiological changes affecting the red blood cell after invasion by malaria parasites,” *Biosens Bioelectron*, vol. 24, no. 8, pp. 2721–2725, Apr. 2009.

[11] M. A. Danzer, “Generalized distribution of relaxation times analysis for the characterization of impedance spectra,” *Batteries*, vol. 5, no. 3, Sep. 2019.

CHAPTER 2

Development of Early-stage Malaria Treatment and Diagnosis by Hybrid Drugs & Electrical Impedance Spectroscopy

2.0 Development of Early-stage Malaria Treatment and Diagnosis by Hybrid Drugs & Electrical Impedance Spectroscopy

2.1 Early-stage malaria treatment

2.1.1 Artesunate-3-chloro-4-(4-chlorophenoxy) aniline hybrid drug

Artesunate 4-Chlorophenoxy Aniline (ATSA) was synthesized by hybridizing artesunate (ATS) and 3-chloro-4-(4-chlorophenoxy) aniline (ANI) through a sequential coupling solvent extraction process as shown in Fig. 2.1. The proposed mechanism of action of ATS is mainly by iron-dependent formation of ATS-heme adducts that block the conversion of heme to less toxic hemozoin crystals. The accumulation of the adducts in the food vacuole leads to parasite death [1] whereas ANI targets the fatty acid type II biosynthesis pathway in mitochondrion by inhibiting a vital *P. falciparum* enzyme; enoyl acyl carrier protein reductase (Pf. EACP) which catalyzes a NADH-dependent reduction of trans-2-enoyl-ACP to acyl-ACP [2]. Targeting the malaria parasites using drugs possessing different mechanisms of action or targets has been shown to have the ability to prolong the lifespan of each drug by providing a protective advantage which in the long run would delay the emergence of resistant parasites [3], [4]. Fig. 2.2a and b show conventional ACTs and their proposed mechanism of action compared with the hybrid drug (ATSA).

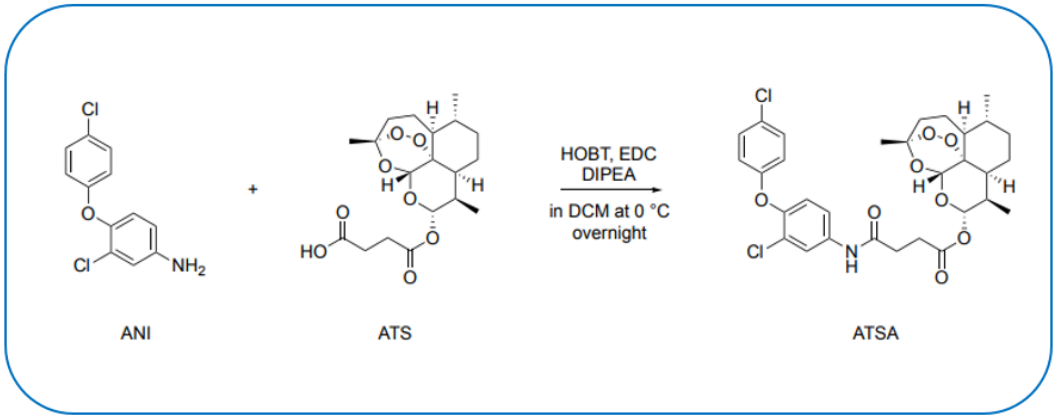

ANI: 3-Chloro-4-(4-chlorophenoxy) aniline, ATS: Artesunate, HOBT: 1-Hydroxybenzotriazole, EDC: 1-Ethyl-3-(dimethylaminopropyl) carbodiimide, DIPEA: N, N-Diisopropylethylamine, DCM: Dichloromethane

Fig.2.1. Synthesis of Artesunate 4-Chlorophenoxy Aniline (ATSA)

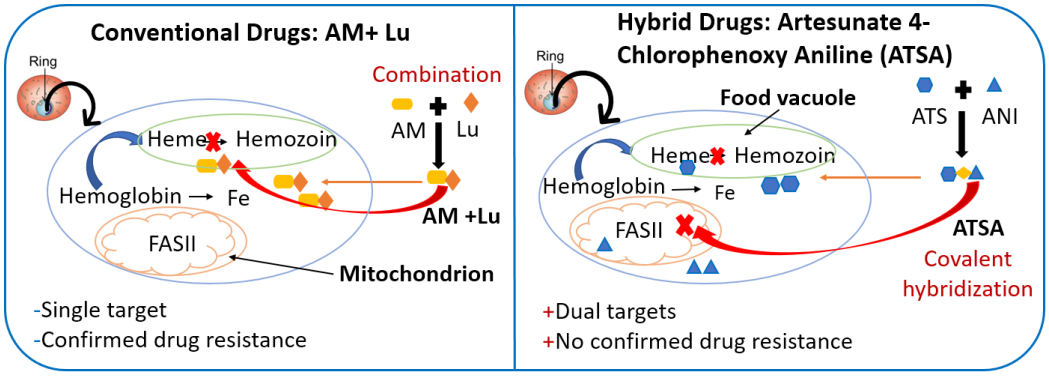

(a) (b)

AM: Artemether, Lu: Lumefantrine, ANI: Aniline; ATS: Artesunate, Fatty acid type II biosynthesis pathway, Fe: Iron

Fig.2.2. Concept of hybrid drugs and their mechanism of action a) Typical drugs; Artemether-lumefantrine, and b) Hybrid drugs: Artesunate 4-Chlorophenoxy Aniline (ATSA)

2.1.2 Overview of artemisinin resistance

Artemisinin (ART) resistance is conferred by a single nucleotide polymorphism in the *P. falciparum* Kelch 13 (PfK13) protein. Si et al have shown that the PfK13 C580Y mutation is associated with reduced endocytosis of hemoglobin from the red blood cell cytoplasm into the parasite and lower requirements of heme and iron (Fe) by the parasite, which causes a decrease in ART activation. Therefore, the parasites become less susceptible to the drug during the ring stage of the intraerythrocytic cycle. In addition, the mitochondrial metabolism allows the parasites to undergo temporary quiescence and once the drug pressure is eliminated, they recover through accelerated growth hence the delay in parasite clearance [5]. The aftermath of parasite survival following the standard 3-day treatment regimen (artemisinin resistance) places enormous drug selection pressure on the long-acting partner drug threatening the overall efficacy of the ACTs. The key to understanding resistance to ACTs (artemisinin derivatives) calls for a clear insight into resistance mechanisms and intrinsic features that would allow the mutant parasites to survive and possibly outcompete the drug-sensitive parasites [6]. Therefore, it is

important to artificially select resistant parasites to standard drugs and evaluate their survival rate (fitness) without drug pressure to monitor how fast natural drug resistance would occur in the population. Fig. 2.3a shows the antimalarial efficacy of artemether in wild-type (sensitive) parasites (AM^S) and Fig. 2.3b decreased efficacy in parasites with the PfK13 mutation (AM^R) respectively.

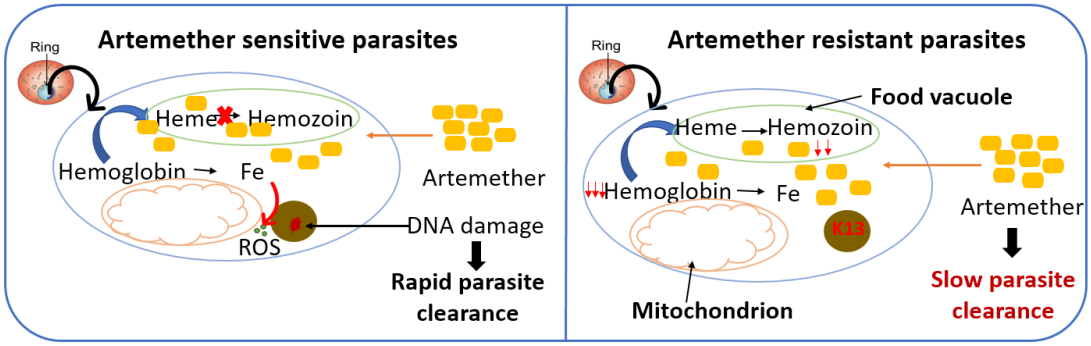

(a) (b)

ROS: Reactive oxygen species, Fe: Iron, K13: Kelch13 mutation

Fig.2.3. Concept of Artemether resistance a) Artemether sensitive parasites, and b) Artemether resistant parasites with kelch-13 mutation.

2.2 Early-stage malaria diagnosis methods

2.2.1 Overview of electrical impedance spectroscopy and distribution of relaxation times (EIS-DRT)

Electrical impedance spectroscopy (EIS) is an analytical and label-free technique in which a small current or voltage signal is applied to a test sample, and the impedance response is measured over a wide range of frequencies. The impedance spectra are represented using a Bode plot which comprises two separate plots of either impedance magnitude or phase angle against frequency [7]. In most cases, the impedance data is interpreted by fitting it to a complex equivalent circuit model (ECM) that requires prior information about the electrical properties of the test samples [8], [9]. The distribution of relaxation times (DRT) analysis provides a simple alternative data analysis method because of its high temporal resolution [10]. The results are easily interpreted since they

are displayed as peaks with distinct relaxation time constants associated with separate polarization processes [11]. Fig. 2.4 shows plots of EIS and DRT analysis.

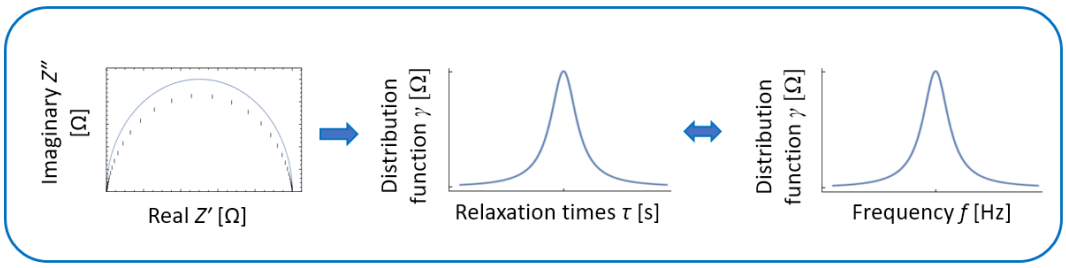

Fig.2.4. Concept of EIS-DRT analysis

References

[1] P. M. O'Neill, V. E. Barton, and S. A. Ward, "The molecular mechanism of action of artemisinin - The debate continues," *Molecules*, vol. 15, no. 3, pp. 1705–1721, Mar. 2010.

[2] M. Wekesa Sifuna, M. Wambui, J. Kang'ethe Nganga, D. Wainaina Kariuki, F. T. Kimani, and F. W. Muregi, "Antiplasmodial Activity Assay of 3-Chloro-4-(4-chlorophenoxy) Aniline Combinations with Artesunate or Chloroquine in Vitro and in a Mouse Model," *Biomed Res Int*, vol. 2019, 2019.

[3] F. W. Muregi and A. Ishih, "Next-generation antimalarial drugs: Hybrid molecules as a new strategy in drug design," Feb. 2010.

[4] B. Meunier, "Hybrid molecules with a dual mode of action: Dream or reality?" *Acc Chem Res*, vol. 41, no. 1, pp. 69–77, Jan. 2008.

[5] W. Si *et al.*, "What exactly does the PfK13 C580Y mutation in Plasmodium falciparum influence?" *Parasit Vectors*, vol. 16, no. 1, Dec. 2023.

[6] M. Duffey, B. Blasco, J. N. Burrows, T. N. C. Wells, D. A. Fidock, and D. Leroy, "Assessing risks of Plasmodium falciparum resistance to select next-generation antimalarials," Aug. 01, 2021, *Elsevier Ltd*.

[7] H. S. Magar, R. Y. A. Hassan, and A. Mulchandani, "Electrochemical impedance spectroscopy (Eis): Principles, construction, and biosensing applications," Oct. 01, 2021, *MDPI*.

[8] H. Bao *et al.*, "Quantitative evaluation of burn injuries based on electrical impedance spectroscopy of blood with a seven-parameter equivalent circuit," *Sensors*, vol. 21, no. 4, pp. 1–8, Feb. 2021.

[9] P. Jash, R. K. Parashar, C. Fontanesi, and P. C. Mondal, "The Importance of Electrical Impedance Spectroscopy and Equivalent Circuit Analysis on Nanoscale Molecular Electronic Devices," Mar. 01, 2022, *John Wiley and Sons Inc*.

[10] M. A. Danzer, “Generalized distribution of relaxation times analysis for the characterization of impedance spectra,” *Batteries*, vol. 5, no. 3, Sep. 2019.

[11] B. A. Boukamp, “Distribution (function) of relaxation times, successor to complex nonlinear least squares analysis of electrochemical impedance spectroscopy?” Oct. 01, 2020, *IOP Publishing Ltd*.

CHAPTER 3

Development of Hybrid Drugs: Artesunate 4-Chlorophenoxy Aniline (ATSA)

3.0 Development of Hybrid Drugs: Artesunate 4-Chlorophenoxy Aniline (ATSA)

3.1 Research Motivation

Malaria is still a major public health burden in many malaria-endemic countries. Approximately 249 million cases and 608,000 deaths were reported in 2022 with the WHO Sub-Saharan African region accounting for 94% of the cases [1]. *Plasmodium vivax*; the most widespread species in the Asia Pacific and South America [2] and *Plasmodium falciparum* [3] the most virulent and highly prevalent in the Sub-Saharan African settings [4] are the major parasite species responsible for global incidences of malaria. Acquired immunity which develops after a few episodes of infections [5] is short-lived [6] and the only approved malaria vaccines for children; RTS, S/AS01, and R21/Matrix-m [7] provide partial immunity. Therefore, chemotherapy is the mainstay of malaria control efforts [8] even though this strategy is extremely hampered by existing *P. falciparum*, *P.vivax*, and *P. malariae* resistant strains in almost all malaria drugs [9]. Consequently, hybrid drugs have been proposed as an alternative to conventional artemisinin-based combination therapies (ACTs) to overcome this setback.

3.2 Hybrid drugs

Hybrid drugs are synthesized by linking two compounds with individual mechanisms of action into a single molecule, a concept known as covalent biotherapy [10]. These compounds have been shown to exhibit enhanced chemotherapeutic profiles [11] such as reduced drug toxicity, increased therapeutic outcomes, improved dosage compliance by the patients [12], [13], and high parasite selectivity [14] due to the synergistic output of the hybridized molecules. Furthermore, the likelihood of parasites developing resistance to these compounds is delayed since individual molecules target the parasites using different mechanisms of action [10], [13].

Several hybrid drugs have been developed since the inception of covalent biotherapy. For instance, PA1103-SAR116242 which reached clinical trials showed improved antimalarial potency against chloroquine-resistant and pyrimethamine-resistant malaria strains; it acts by inhibiting hemozoin bio-crystallization (aminoquinoline moiety) and alkylating heme molecules [11]. A trioxaquine hybrid comprising artesunate and 4,7-dichloro quinoline manifested superior antimalarial efficacy in a cerebral malaria mice

model compared to its precursors [15]. Moreover, mefloquine-artesunate hybrid (MEFAS) manifested improved potency compared to single molecules *in vitro* on *P. falciparum* W2 and 3D7 clones and *in vivo* on *P. berghei* NK65 strain, *P. falciparum* sensitive (D6) and resistant (W2) clones [16]. In this study, artesunate-3-chloro-4-(4-chlorophenoxy) aniline (ATSA) hybrid drug is synthesized via covalent linkage of artesunate (ATS) and 3-chloro-4-(4-chlorophenoxy) aniline (ANI) through a sequential coupling solvent extraction. Antimalarial activities are then determined *in vitro* using *P. falciparum* (3D7) strain and in mice using *P. berghei* ANKA (sensitive) and *P. berghei* lumefantrine resistant (LuR) parasites. The Pre-ADMET online tool predicted the absorption, distribution, metabolism, excretion, and toxicity (ADMET) profiles in silico. Artesunate (ATS) was used as a reference drug.

3.3 Experiment

3.3.1 Malaria parasites, Vero cells, test drugs, and experimental mice

P. falciparum 3D7 strain, *P. berghei* ANKA, and *P. berghei* lumefantrine resistant (LuR) parasites were used for *in vitro* and *in vivo* assays respectively. Cryopreserved *P. berghei* parasites were revived by initially thawing, centrifuging, and injecting into two groups (*P. berghei* ANKA and *P. berghei* LuR) of two mice each using a needle of size 26G ×5/8″ through the intraperitoneal route (i.p). The parasites were passaged every week into naive mice to resuscitate their virulence. These infected mice were donors for setting the standard 4-day suppressive tests (4-DT) and curative tests after establishing a steady state parasitemia. The Vero E6 cell line was used for cytotoxicity assays.

Artesunate (ATS) and 3-chloro-4-(4-chlorophenoxy) aniline (ANI) were purchased from Sigma Aldrich ® while ATSA was synthesized by hybridizing the two compounds via a solvent extraction process.

Randomly bred Swiss albino mice, 5 to 6 weeks old, same-sex weighing 20±2 g randomly distributed into three or five mice in each group (separate male or female), clearly labeled with experimental details, and fed on commercial rodent food and water ad libitum were maintained in an animal house experimental room in standard polypropylene (hard plastic) cages. All measures were taken to minimize animal suffering throughout the experiments following international laws and regulations regarding the use of experimental animals.

3.3.2 Experimental methods

3.3.2.1 Antiplasmodial and cytotoxicity assays

P. falciparum parasites were cultured using the Trager and Jensen method with slight modifications [18]. Fig. 3.1a shows the screening of ATSA for antiplasmodial activity. Briefly, 25 µl complete culture medium was added to all wells. Twenty-five microliters of either ATSA or TSA drugs were then added. A serial two-fold dilution over a 64-fold concentration range was carried out using a motorized hand diluter. Two hundred microliters of parasitized RBCs at 0.4% parasitemia were added to test wells. Into some control wells, 200 µl of non-parasitized RBCs was added. The plates were placed in an air-tight gas chamber, gassed with 3% CO_2, 5% O_2, and 92% N_2, and incubated for 72 h at 37 °C. Each specific well was then pulsed with 25 µl of culture medium containing 0.5 µCi of [^{3}H] hypoxanthine and the plates were incubated for 18 h. The contents of each well were harvested in glass fiber filters and washed several times, and radioactivity was measured in counts per minute using a liquid scintillator [19]. The 50% inhibitory concentration (IC_{50}) was obtained by nonlinear probit or regression of percentage growth inhibition for each drug.

The Mosmann, 3-(4,5-dimethylthiazol-2-yl)- 2,5-diphenyltetra-zolium bromide (MTT) cell viability assay was used for cytotoxicity assay *in vitro* [17]. Briefly, 100 µl of cell suspension at a density of 2×10^4 was seeded into 96-well fat-bottomed microtiter plates. The culture plates were then incubated at 37 °C with 5% CO_2 for 24 h, 150 µl of the test drugs was added, and a triplicate dilution was performed. The plates were again incubated for 24 h before 10 µl of 5 mg/ ml MTT solution was added to each well to give a final concentration of 0.5 mg/ml. The plates were incubated for a further 4 h then 100 µl dimethyl sulfoxide (DMSO) was added to dissolve formazan crystals and the absorbance was read at 562 nm/690 nm using a scanning multi-well spectrophotometer (Multi-scan EX Lab-systems) as shown in Fig. 3.1b. Data was entered in a MICROSOFT EXCEL software and the inhibitory concentration that causes the death of 50% of cells (CC_{50}) was determined using Eq. 3.1.

$$CC_{50} = \frac{(Absorbance_{562} - Absorbance_{690})test}{(Absorbance_{562} - Absorbance_{690})control} \times 100 \quad (3.1)$$

The selective index was determined by Eq. 3.2.

$$SI = \frac{CC_{50\ of\ Vero\ cells}}{IC_{50\ of\ 3D7\ parasites}} \quad (3.2)$$

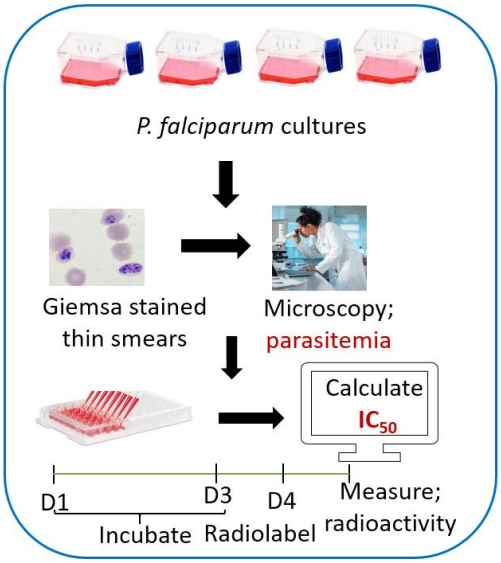

Fig.3.1a. *In vitro* antiplasmodial assay

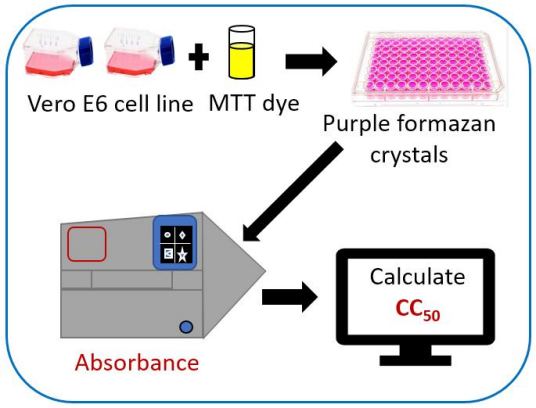

Fig.3.1b. *In vitro* cytotoxicity assay

3.3.2.2 Early infection and curative assays

The standard 4-day chemo-suppressive tests (4DTs) were used in early infection tests to assess the percentage reduction in parasitemia in mice injected with *P. berghei* ANKA, and LuR iRBCs [20] as shown in Fig. 3.2a. Briefly, infected mice were distributed randomly into three test dose groups and a negative control group of five mice each. Freshly prepared drug solutions, 200 µl was administered orally to the mice at a time t = 3 h, 24 h, 48 h, and 72 h post-infection (p.i) using a stainless steel, 24-gauge feeding cannula (Harvard Apparatus; 25 mm in length, 1.25 mm ball diameter). Negative controls received distilled water. On day 5 (D_5) pi, thin blood smears from mice tail snips were prepared, and fixed by immersing the slides in absolute methanol for 30 s, air-dried, stained with 10% working Geimsa solution for 20 min, washed over running tap water and dried at the extreme edge of the hood. A drop of immersion oil was placed on the smears and parasites were examined using a microscope (OLYMPUS X3) at ×1000

magnification. Parasite load (percentage parasitemia; PP) from four random microscope fields was calculated using Eq. 3.3.

$$PP = \frac{T_{iRBC}}{T_{RBC}} \times 100 \quad (3.3)$$

T_{iRBC} is the total number of infected RBCs while T_{RBC} is the total number of RBCs. Percentage parasitemia suppression (PPS) (chemo-suppression) was determined using Eq. 3.4.

$$PPS = \frac{A-B}{A} \times 100 \quad (3.4)$$

A is the mean parasitemia in the negative control group while B is the mean parasitemia in test groups.

Fig. 3.2b shows the experimental method for the curative tests. Mice were injected i.p with the *P. berghei* ANKA iRBCs and randomized into the test and negative control groups of five mice each. Smears were made on D_4 post-infection just before the start of treatment to confirm infection and determine initial parasitemia. Drug solutions equivalent to ED_{50}s of ATSA obtained in early infection tests were administered on D_4, D_5, and D_6. Smears were made on D_7, D_9, D_{11}, and D_{13} to monitor the reduction in parasitemia. Percentage parasitemia was determined as previously described and average percentage suppression (APS) of parasitemia was determined using Eq. 3.5:

$$APS = \frac{PD_4}{PD_7} \times 100 \quad (3.5)$$

PD_4 is the average % parasitemia before treatment, day 4, while PD_7 is the average % parasitemia at day 7 after treatment.

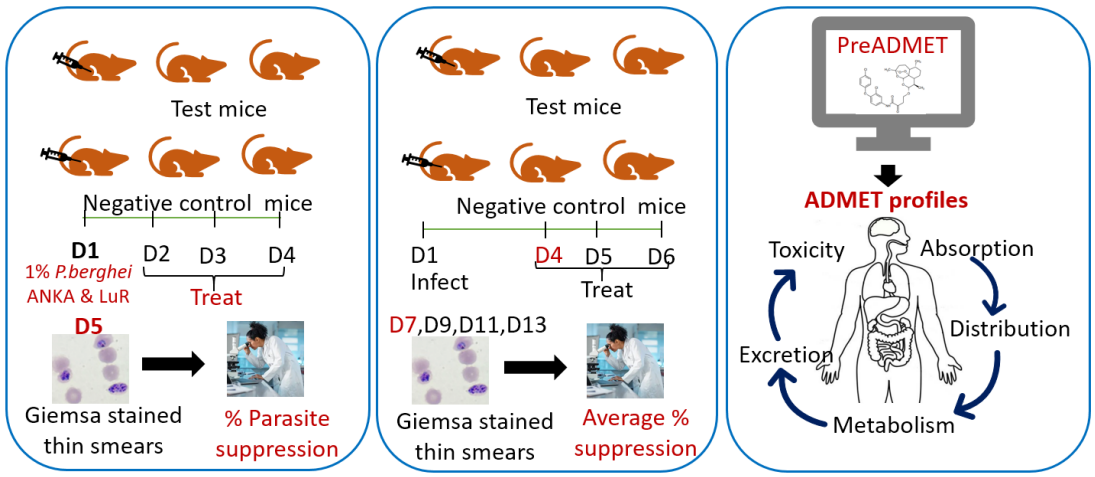

Fig.3.2. *In vivo* antimalarial activity and in silico prediction of ADMET profiles of Artesunate 4-Chlorophenoxy Aniline. a) Early infection tests b) Curative tests, and c) ADMET profiles.

3.3.2.3 Prediction of ADMET profiles

ADMET profiles were predicted in silico using the Pre-ADMET online prediction tool. The 2D structures of ATSA and ATS were drawn using an online user interphase Chem-Doodle® drawing tool in the Pre-ADMET server and directly submitted to calculate the following parameters: absorption, distribution, metabolism, and toxicity.

3.4 Experimental results

3.4.1 Cytotoxicity and antiplasmodial activity

The 50% inhibitory concentration for Vero cells (CC_{50}) and the 50% inhibitory concentration (IC_{50}) for *P. falciparum* parasites were 25.015 ± 2.325 µg/ml and 11.47 ± 1.3 ng/ml for ATSA, and 48.945 ± 0.035 µg/ml and 2.00 ± 0.93 ng/ml for ATS, respectively. The selective index (SI) was 2180.91 and 42,475 for ATSA and ATS respectively.

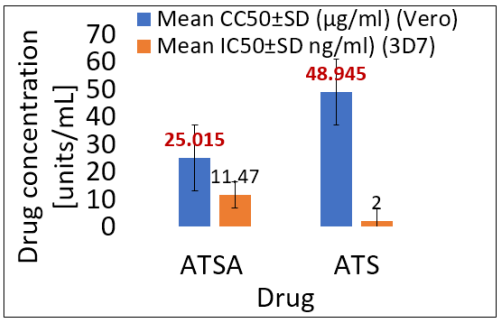

Fig.3.3. *In vitro* cytotoxicity and antiplasmodial inhibitory drug concentrations.

3.4.2 Early infection and curative tests

The early infection test results demonstrate a dose-dependent relationship. In *P. berghei* ANKA, parasite chemo-suppression after a 3.0 mg/kg body weight was 41.47% for ATSA. ATSA suppressed *P. berghei* LuR parasites by 63.30% as shown in Fig. 3.4a. Compared to the controls, the percentage activities of ATSA in *P. berghei* ANKA and *P. berghei* LuR were statistically significant $P < 0.05$. The fifty percent effective inhibitory dosages (ED_{50}s) were 4.211 mg/kg/day, 2.601 mg/kg/day for ATSA, and 2.108 mg/kg/day, 1.883 mg/kg/day for ATS against *P. berghei* ANKA and *P. berghei* LuR parasites respectively as shown in Fig. 3.4b.

The average percentage chemo-suppression of ATSA in the curative test against *P. berghei* ANKA was determined on D_7 in mice treated for 3 days (D_4 to D_6) with the ATSA's ED_{50} value of 4.211 mg/kg/day obtained in the early infection test. The results demonstrate that the percentage of chemosuppression was statistically significant $P < 0.05$. Figure 3.5 shows the average parasitemia between D_4 and D_{13} where the parasitemia decreased gradually till D_7 and afterwards began to rise.

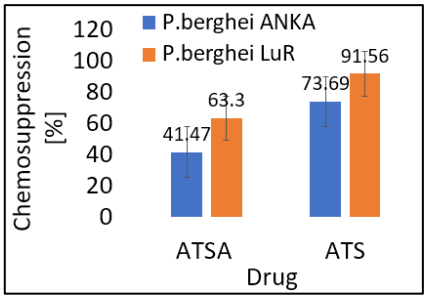

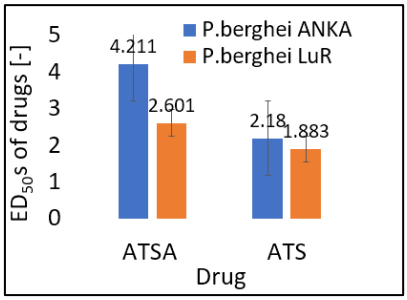

(a) (b)

Fig.3.4. *In vivo* antimalarial activity in early infection test. a) Parasite suppression (%), and b) Fifty percent effective inhibitory dosages ($ED_{50}s$).

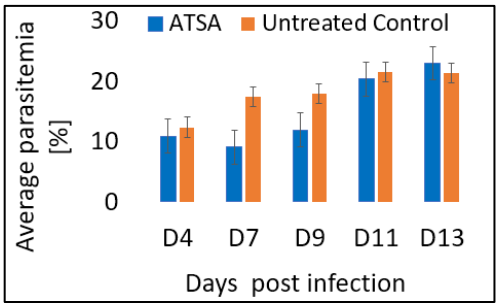

Fig.3.5. *In vivo* antimalarial activity in a curative test.

3.4.3 ADMET profiles of ATSA hybrid drug

Table 1 summarizes the ADMET profiles of ATSA which shows that most parameters are similar to those of the reference drug ATS.

3.4.3.1 Absorption profile

The human intestinal absorption (HIA), permeability to the human epithelial colorectal adenocarcinoma (Caco-2) cells, the Mandin-Darby canine kidney (MDCK) cells, P-glycoprotein (P-gp) inhibition, and skin permeability profiles demonstrate the absorption parameters. The ATSA shows a slightly higher HIA value, 96.83% compared to 88.68% for ATS. ATSA also exhibits a remarkably low permeability to MDCK cells (0.070*cm/s) in comparison with 0.34 cm/s for ATS but has a high permeability to Caco-

2 cells (29.86 cm/s) compared to 13.19 cm/s for ATS. ATSA inhibits P-gp and has a skin permeability of -2.54 cm/h while ATS is a non-inhibitor to P-gp with a skin permeability of -3.77 (cm/h) as shown in Table 1.

3.4.3.2 Distribution profile

The distribution profiles of ATSA and ATS were predicted using brain-blood barrier (BBB) penetration and percentage plasma protein binding (PPB) parameters. ATSA shows a BBB value of 0.36 compared to 0.01 for ATS. The PPB is 91.51% and 70.12% for ATSA and ATS respectively as shown in Table 1.

3.4.3.3 Metabolism profile

Metabolism was determined by screening whether ATSA in comparison with ATS was an inhibitor or a substrate to various members of cytochrome P450 gene (CYP) subfamilies: CYP 2C19 inhibition, CYP 2C9 inhibition, CYP 2D6 inhibition, CYP 3A4 inhibition, CYP 2D6 substrate, and CYP 3A4 substrate using Pre-ADMET predictor. It was found that ATSA is an inhibitor of CYP 2C19, CYP 2C9, and CYP 3A4 and non-substrate to CYP 2D6. ATSA also inhibits CYP 2D6 but is a substrate for CYP 3A4 as shown in Table 1.

3.4.3.4 Toxicity profile

Toxicity was determined by screening for Ames mutagenicity, carcinogenicity in mouse or rat models, and human ether-a-go-go related gene (hERG) potassium ion (K^+) channel inhibition. ATSA shows non-mutagenicity to both TA100 and TA1535 strains similar to ATS. ATSA exhibits medium risk while ATS displays a low inhibition risk of the hERG K^+ channel as shown in Table 1.

Table 1 ADME and Toxicity profiles of ATSA against ATS

Table 1 In silico ADME and toxicity profiles of ATSA against ATS

Target test	Drugs	
	ATSA	**ATS**
HIA (%)	96.83	88.68
Caco-2 (cm/s)	29.86	13.19
MDCK (cm/s)	0.07	0.34
P-gp inhibition	Substrate	Substrate
Skin permeability	- 2.54	-2.74
BBB permeability	0.16	-0.95
PPB (%) permeability	- 1.26	-3.04
CYP 2C19 inhibitor	Inhibitor	Inhibitor
CYP 2C9 inhibitor	Inhibitor	Inhibitor
CYP2D6 inhibition	Inhibitor	Non-inhibitor
CYP2D6 substrate	Non-substrate	Non-substrate
CYP 3A4 inhibition	Inhibitor	Inhibitor
CYP 3A4 substrate	Substrate	Substrate
Ames test	Non- mutagenic	Non- mutagenic
hERG inhibition	Medium risk	Low risk
TA 100_10RLI	Non-mutagen	Non-mutagen
TA 100_NA	Non- mutagen	Non- mutagen
TA 1535_10RLI	Non-mutagen	Non-mutagen
TA 1535_NA	Non- mutagen	Non- mutagen

HIA human intestinal absorption, *Caco-2* human epithelial adenocarcinoma colorectal cell line, *MDCK* Mandin-Darby Canine Kidney cells, *P-gp* P-glycoprotein, *BBB* blood-brain barrier, *PPB* plasma protein binding, *CYP* cytochrome P450 enzymes, *hERG* human ether-a -go-go-related gene, TA *100/1535 Salmonella typhimurium* strain.

3.4 Discussion

The world continues to lose effective antimalarial drugs due to the growing number of multi-drug resistant human malaria parasites. Since malaria continues to cause death mostly to children below the age of 5 years and pregnant women, particularly in sub-Saharan Africa, alternative medications effective to both sensitive and resistant parasites are in constant need. This study thus evaluated the antimalarial activity, toxicity, and in silico ADMET profiles of a novel molecule, artesunate-3-chloro-4(4-chlorophenoxy) aniline (ATSA) hybrid. Artesunate (ATS) was used as a reference drug. The cytotoxicity results revealed that the hybrid drug has a wide safety margin; a selective index (SI) of

2180.91 compared to 42,475 for ATS using the *P.falciparum* 3D7 strain. ATSA exerted significant parasite chemo-suppression to the *P. falciparum* and *P. berghei* parasites, $P < 0.05$. However, the antimalarial activity of ATSA was observed to be less than that of the popular clinically used trioxane drug artesunate. The solubility of ANI was low; possibly limiting its bioavailability and it may be a short-acting drug. Since artesunate is similarly a short-acting drug, this could explain the reduction in the chemosuppression of ATSA. However, its potency may be enhanced through specific slight modifications of the linker as this has been shown to improve the chemotherapeutic outcome of hybrid drugs [21]. ATSA targets the malaria parasites by two distinct mechanisms; ANI is critical in the FAS-II pathway in the apicoplasts [22] whereas artesunate promotes heme alkylation through its 1,2,3-trioxane entity which implies that the development of resistance to this novel hybrid compound might be delayed [23].

Absorption of drugs into the blood systems depends on apical-basolateral (A-B) permeability. Since the intestinal membrane acts as the first barrier to orally administered large and charged molecules [24], poor performance and low drug concentrations in target regions are attributed to limited solubility in aqueous media [25]. A drug penetrates membranes through passive diffusion, active transport, and paracellular transport [26]. Various in silico tools are used to calculate the percentage HIA as a sum of bioavailability and absorption. HIA is evaluated from the ratio of excretion and or cumulative excretion in urine, bile, and feces [27], and the permeability of a compound to either Caco-2 cells or MDCK cells. Caco-2 cells have multiple transport channels through the intestinal epithelia that mimic most transport pathways in gastrointestinal tracts. ATSA exhibited a high percentage HIA of 96.83% and a Caco-2 permeability of 29.86 cm/sec compared to 88.68% and 13.19 cm/s respectively for ATS. ATSA has a remarkably low MDCK cell permeability of 0.07 cm/sec compared to 0.34 cm/s for ATS, suggesting it is highly bioavailable. Transdermal delivery of drugs has a wide range of advantages such as stomach bypass, higher patient compliance, and expeditious administration of drugs with short half-life or narrow therapeutic index among others [28]. Skin permeability index analysis for a new drug is thus important as it indicates whether across-the-skin delivery is possible and the extent of damage likely to occur due to accidental contact with a drug [29]. A negative value for skin permeability of - 2.45 cm/h, ATSA, and - 3.77cm/h of ATS suggest that ATSA cannot penetrate the skin and thus is equally safe as artesunate.

Drug distribution is determined by calculating the BBB penetration and percentage PPB profiles. BBB is the ratio of the concentration of a drug in the brain to its concentration in the blood (C_{brain}/C_{blood}). Plasma protein binding (PPB) of a drug influences its action and disposition as only unbound drug molecules are free to cross membranes by diffusion or active transport as well as for interaction with drug targets [30]. ATSA has considerably higher predicted BBB and PPB values 0.36 and 91.51% respectively compared to 0.01 and 70.12% for ATS. A high BBB value may suggest that ATSA could have potential in the management of cerebral malaria.

Drug metabolism is key to its eventual excretion from the body. The results shown in Table 1 reveal that ATSA is an inhibitor of CYP 2C19, CYP 2C9, and CYP 3A4 genes and a non-substrate to CYP 2D6 genes. It inhibits CYP 2D6 but it is a substrate for CYP 3A4. The predictions suggest that ATSA is safe for humans.

Two strains of *Salmonella typhimurium*, TA100, and TA1535 (+ S9 activated with 10% liver homogenate and -S9 not activated) having mutations in genes responsible for histidine metabolism are used in predicting the Ames test. The Ames test shows that ATSA is non-mutagenic to the TA100 strain of bacteria. The hERG K^+ channels are predominately expressed in cardiac muscles and the blockade of these channels by drugs induces acquired long QT syndrome that may trigger arrhythmias [31]. ATSA exhibits medium hERG K^+ channel inhibition risk suggesting that it is safe.

3.5 Summary

The antimalarial activity of Artesunate 4-Chlorophenoxy aniline (ATSA) is evaluated using *in vitro Plasmodium falciparum* and *P. berghei* parasites in mice, and the absorption, distribution, metabolism, excretion, and toxicity (ADMET) profiles in silico are predicted using Pre-ADMET online tool.

The results demonstrate that ATSA has;

1. Antiplasmodial activity *in vitro* of 11.47±1.3 ng/ml
2. Wide safety margin: Selective index (SI) > 2000.
3. Antimalarial chemosuppression activity *in vivo* of > 40%.
4. High predicted human intestinal absorption (HIA), > 95%
5. Medium predicted human ether-a-go-go-related gene (hERG) K^+ channel inhibition risk.

References

[1] W. Health Organization, *World Malaria Report 2022*. 2023. [Online].

[2] F. Angrisano and L. J. Robinson, "*Plasmodium vivax* – How hidden reservoirs hinder global malaria elimination," *Parasitol Int*, vol. 87, Apr. 2022.

[3] B. Hermansyah *et al.*, "Clinical features of severe malaria: Protective effect of mixed plasmodial malaria," *Asian Pac J Trop Biomed*, vol. 7, no. 1, pp. 4–9, Jan. 2017.

[4] M. Tachibana *et al.*, "*Plasmodium vivax* transmission-blocking vaccines: Progress, challenges, and innovation," *Parasitol Int*, vol. 87, Apr. 2022.

[5] H. Joseph, E. Eriksson, and L. Schofield, "Early suppression of B cell immune responses by low doses of chloroquine and pyrimethamine: implications for studying immunity in malaria," *Parasitol Res*, vol. 118, no. 6, pp. 1987–1992, Jun. 2019.

[6] N. Horata, K. Choowongkomon, S. Ratanabunyong, J. Tongshoob, and S. Khusmith, "Acquisition of naturally acquired antibody response to *Plasmodium falciparum* erythrocyte membrane protein 1-DBLα and differential regulation of IgG subclasses in severe and uncomplicated malaria," *Asian Pac J Trop Biomed*, vol. 7, no. 12, pp. 1055–1061, Dec. 2017.

[7] W. Health Organization, "World Malaria Report 2022." [Online]. Available: https://www.who.int/teams/global-malaria-programme.

[8] M. Dhanawat, N. Das, R. Nagarwal, and S. Shrivastava, "Antimalarial Drug Development: Past to Present Scenario," *Mini-Reviews in Medicinal Chemistry*, vol. 9, no. 12, pp. 1447–1469, Nov. 2009.

[9] L. S. Feng *et al.*, "Hybrid molecules with potential *in vitro* antiplasmodial and *in vivo* antimalarial activity against drug-resistant *Plasmodium falciparum*," May 01, 2020, *John Wiley and Sons Inc*.

[10] F. W. Muregi and A. Ishih, "Next-generation antimalarial drugs: Hybrid molecules as a new strategy in drug design," Feb. 2010.

[11] B. Meunier, "Hybrid molecules with a dual mode of action: Dream or reality?" *Acc Chem Res*, vol. 41, no. 1, pp. 69–77, Jan. 2008.

[12] M. C. Lombard *et al.*, "Potent *in vivo* anti-malarial activity and representative snapshot pharmacokinetic evaluation of artemisinin-quinoline hybrids," *Malar J*, vol. 12, no. 1, 2013.

[13] A. Nilsen *et al.*, "Discovery, synthesis, and optimization of antimalarial 4(1 H)-quinolone-3-diaryl ethers," *J Med Chem*, vol. 57, no. 9, pp. 3818–3834, May 2014.

[14] M. Sharma *et al.*, "Design and synthesis of a new class of 4-aminoquinolinyl- and 9-anilinoacridinyl schiff base hydrazones as potent antimalarial agents," *Chem Biol Drug Des*, vol. 84, no. 2, pp. 175–181, 2014.

[15] O. C. Odhiambo *et al.*, "Efficacy and safety evaluation of a novel trioxaquine in the management of cerebral malaria in a mouse model," *Malar J*, vol. 16, no. 1, Jul. 2017.

[16] F. D. P. Varotti *et al.*, "Synthesis, antimalarial activity, and intracellular targets of MEFAS, a new hybrid compound derived from mefloquine and artesunate," *Antimicrob Agents Chemother*, vol. 52, no. 11, pp. 3868–3874, Nov. 2008.

[17] T. Mosmann, "Rapid Colorimetric Assay for Cellular Growth and Survival: Application to Proliferation and Cytotoxicity Assays," 1983.

[18] "Trager & Jensen".

[19] M. F. Khan *et al.*, "The natural anti-tubercular agents: In silico study of physicochemical, pharmacokinetic and toxicological properties," *J Appl Pharm Sci*, vol. 7, no. 5, pp. 34–38, May 2017.

[20] S. K. Kimani, J. K. Nganga, D. W. Kariuki, J. Kinyua, F. T. Kimani, and D. M. Kiboi, "*Plasmodium berghei* ANKA: Selection of pyronaridine resistance in a mouse model," *African Journal of Biochemistry Research*, vol. 8, no. 6, pp. 111–117, Aug. 2014.

[21] N. S. Dambuza *et al.*, "Antiplasmodial activity, *in vivo* pharmacokinetics and anti-malarial efficacy evaluation of hydroxypyridinone hybrids in a mouse model," *Malar J*, vol. 14, no. 1, Dec. 2015.

[22] M. Wekesa Sifuna, M. Wambui, J. Kang'ethe Nganga, D. Wainaina Kariuki, F. T. Kimani, and F. W. Muregi, "Antiplasmodial Activity Assay of 3-Chloro-4-(4-chlorophenoxy) Aniline Combinations with Artesunate or Chloroquine *in vitro* and in Mouse Model," *Biomed Res Int*, vol. 2019, 2019.

[23] F. Dé Ric Coslé Dan *et al.*, "Selection of a trioxaquine as an antimalarial drug candidate," 2008. [Online]. Available: www.pnas.org/cgi/content/full/

[24] I. Gessner and I. Neundorf, "Nanoparticles modified with cell-penetrating peptides: Conjugation mechanisms, physicochemical properties, and application in cancer diagnosis and therapy," *Int J Mol Sci*, vol. 21, no. 7, Apr. 2020.

[25] Y. Mehmood *et al.*, "*In-vitro* and *in-vivo* evaluation of velpatasvir-loaded mesoporous silica scaffolds. A prospective carrier for drug bioavailability enhancement," *Pharmaceutics*, vol. 12, no. 4, Apr. 2020.

[26] T. Knöpfel *et al.*, "Paracellular transport of phosphate along the intestine," *Am J Physiol Gastrointest Liver Physiol*, vol. 317, pp. 233–241, 2019.

[27] M. Zhao *et al.*, "Cytochrome p450 enzymes and drug metabolism in humans," Dec. 01, 2021, *MDPI*.

[28] R. Parhi and A. Mandru, "Enhancement of skin permeability with thermal ablation techniques: concept to commercial products," Jun. 01, 2021, *Springer*.

[29] N. S. R. Silva *et al.*, "Computational Analysis of Physicochemical, Pharmacokinetic and Toxicological Properties of Deoxyhypusine Synthase Inhibitors with Antimalarial Activity," *Comput Mol Biosci*, vol. 04, no. 04, pp. 47–57, 2014.

[30] C. Dohutia, D. Chetia, K. Gogoi, D. R. Bhattacharyya, and K. Sarma, "Molecular docking, synthesis and in vitro antimalarial evaluation of certain novel curcumin analogues," *Brazilian Journal of Pharmaceutical Sciences*, vol. 53, no. 4, 2017.

[31] M. C. Sanguinetti, "HERG1 channel agonists and cardiac arrhythmia," *Curr. Opin. Pharmacol*, vol.15, pp.22-27, Apr.2014.

CHAPTER 4

Evaluation of artemether resistance and survival rate

4.0 Evaluation of artemether resistance and survival rate

4.1 Research Motivation

Increasing failure rates threaten the clinical use of artemisinin-based combination therapies (ACTs) due to the emergence and spread of multiple drug-resistance genes in most human plasmodium strains [1]. In ACTs, the artemisinin derivative is a short-acting drug while the partner drug is a long-acting drug [2]. These combinations constitute a minor problem in low-transmission settings, but their successful use remains a major challenge in high-transmission areas [3] due to their pharmacokinetic mismatch. The strong selection pressure presented by the long-acting antimalarial drugs, especially at sub-therapeutic levels, portends that selection of re-infecting resistant parasites may occur rapidly in African regions with a high incidence of malaria and where antimalarial drugs are widely misused [4]. To sidestep this setback there is a need to understand the resistance mechanisms. Artemether is among the derivatives of artemisinin and is a component in artemether-lumefantrine (Coartem®) ACT [5], [6].

4.2 Clinical resistance to artemisinin

Cases of reduced susceptibility of *P. falciparum* to artemisinin emerged more than 15 years ago [7]. In Cambodia where resistance to the long-acting partner drugs piperaquine and mefloquine exists, increased treatment failure rates to dihydroartemisinin-piperaquine led to the re-introduction of artesunate-mefloquine which had been withdrawn following the emergence of its resistance barely a decade after its adoption for clinical use [8], [9]. Clinical resistance to artemisinin, defined as a prolonged parasite clearance time [8], [10], recurrence of infection after 3 days of effective treatment [2], and treatment failure rate [11] mainly conferred by single nucleotide polymorphisms in the *Pf*K13 propeller region [8], [12], was first reported in Pailin, western Cambodia [9] and later spread to or emerged separately in other parts of the Greater Mekong Subregion [8] such as north-western Thailand and southern Myanmar [13].

It is of major concern that artemisinin resistance could spread outside the Greater Mekong Subregion due to the past trends of the emergence of chloroquine and sulfadoxine-pyrimethamine resistance in these regions before migrating to Africa [14]. It is predicted that the aftermath of the emergence and spread of resistance to artemisinin in Sub-Saharan Africa would be more devastating, would place a huge economic burden on

the resource-constrained malaria-endemic countries, and would result in massive mortality [11]. This would, in turn, curtail global efforts directed towards malaria control and elimination [8]. Recently, gene mutations linked to the delay in the clearance of *P. falciparum* parasites, observed to arise independently in Africa, have been reported in Uganda and Rwanda. Cross-sectional surveys of isolates collected from malaria patients in Uganda have revealed the presence of reduced artemisinin-susceptible *P. falciparum* parasites showing high survival rates [14]. Another study in Rwanda reported a higher prevalence of the *Pf*K13 R561H mutation in some patient samples [8] obtained from one of the three study sites compared with research findings from a previous study conducted in Uganda, Rwanda, and Tanzania [12].

4.2.1 Artemether resistance

Drug-resistant lines can be induced *in vitro* using *P. falciparum* or *in vivo* using *P. berghei* parasites [15]. The selection of drug resistance *in vitro* is a long, expensive process, and the stability of resistant phenotypes is intricate to establish [15]. Several studies have demonstrated that *in vivo* antimalarial drug resistance can be achieved easily in malaria mice models [16], [17]. Previously, stable *P. vinckei* chloroquine-resistant parasites and unstable *P. berghei* ANKA artemisinin-resistant parasites [18], and stable *P. chabaudi* artemisinin- and artesunate-resistant clones expressing a single nucleotide polymorphism in the ubiquitin-binding protein 1 gene [19] have been selected using the continuous drug pressure technique. However, the generation of *P. berghei* ANKA artemether-resistant parasites through constant exposure to single high doses selected for parasites exhibiting a swift loss of drug tolerance upon removal of drug selection pressure [18].

4.2.2 Survival rate

Although parasite virulence is influenced by various human host, parasite, mosquito vector, and epidemiological factors [8], the Darwinian virulence evolutionary hypothesis postulates that natural or induced (through serial passages) selection and adaptation of parasites promote their virulence and thus their survival rate (fitness cost), which, in turn, enhances optimum lifelong disease transmission [20]. A comparative study using *P. chabaudi* cloned parasite lines in a mouse model demonstrated that clones with more effective multiplication rates manifested enhanced virulence and more efficient disease

transmission to mosquitoes [21]. A similar study using *P. falciparum* parasites found that El Limon, a strain from Panama (high-transmission zone), exhibited higher virulence and malaria transmissibility to mosquitoes compared with Santee-Cooper, a strain from South Carolina (low-transmission zone). Host immunity has been shown to play a vital role in the selection and transmissibility of virulent parasites although the exact mechanism through which this occurs is not yet clearly understood [21]. Therefore, the survival rate (fitness cost) of a moderately stable AM^R parasite line generated by continuous drug pressure doses for 9 months in a mouse model using *P.berghei* ANKA (parental strain/AM^S) parasites was assessed.

4.3 Experiment

4.3.1 Experimental mice

Swiss male albino mice weighing 20 ± 2 g were injected intraperitoneally (i.p.) with blood obtained from donor mice cardiac puncture containing approximately 0.5% *P.berghei* ANKA infected red blood cells (iRBCs) in 0.2 mL of phosphate saline with glucose (PSG) inoculum. The mice were randomized into test and control groups, housed in plastic cages, fed on normal pellets and water ad libitum, and maintained in the animal facility [22].

4.3.2 Experimental methods

4.3.2.1 Determination of ED_{50} and ED_{90} of *P.berghei* ANKA (sensitive) strain

Effective doses that reduce parasitemia by 50% and 90% (ED_{50} and ED_{90}) respectively for artemether against the parental strain were evaluated using the standard 4-day suppressive test. Twenty mice were injected i.p. with *P. berghei* ANKA iRBCs on Day 0. The mice were distributed randomly into three test dose groups (2.5, 1.25, and 0.625 mg/kg body weight) and a negative control group (five mice per group). The freshly prepared drug solution was orally (p.o) administered 3h (D1), D2, D3, and D4 h post-infection (pi). On Day 5 (96 h) pi, the level of parasitemia as a percentage of total RBCs was assessed microscopically (Olympus CX31) at × 1000 magnification on prepared Geimsa-stained thin films using the formula in Eq. 4.1:

$$P_p = \frac{RBC_i}{RBC_t} \times 100 \qquad (4.1)$$

where P_p is the percentage parasitemia, RBC_i is the total number of infected RBCs, and RBC_t is the total number of RBCs counted [22]. Data were recorded in Excel (Microsoft Corp., Redmond, WA, USA), and percentage chemosuppression was determined using the formula in Eq. 4.2:

$$P_r = 100 - \left[\frac{A-B}{A}\right] \times 100 \quad (4.2)$$

where P_r is the percentage reduction in parasitemia, A is the mean parasitemia in the negative control group, and B is the mean parasitemia in the test group [23]. ED_{50} was estimated graphically by linear regression using Statistica 2000 Version 5.5.

4.3.2.2 Artemether resistance

Six *P. berghei* ANKA-infected mice were divided into a test group and a negative control group (three mice per group) as shown in Fig. 4.1a. Parasitaemia was monitored until > 0.5% and < 4% was attained. Mice in the test group were treated p.o. with artemether for 3 days at a drug concentration equivalent to ED_{99}, while the mice in the negative control group received distilled water. Continuous artemether drug pressure (AM-DP) was induced for 270 days subject to the growth of parasites. At every passage, three mice were injected i.p. with 0.5% *P. berghei* iRBCs in 0.2 mL of PSG inoculum, and the mice were treated p.o. with the AM-DP dose after attainment of > 0.5% and < 4% parasitemia. The degree of resistance was assessed every 120 days using the 4-day suppressive test to determine the new ED_{50} and ED_{90} [22] and the indices of resistance (I) at 50% and 90% (I_{50} and I_{90},) respectively by the ratio of ED_{50} or ED_{90} of the AM^R line to that of the AM^S strain, respectively using Eqs. 4.3 and 4.4 [17].

$$I_{50} = \left[\frac{ED_{50}\ Resistance\ line}{ED_{50}\ Parent\ line}\right] \quad (4.3)$$

$$I_{90} = \left[\frac{ED_{90}\ Resistant\ line}{ED_{90}\ Parent\ line}\right] \quad (4.4)$$

Resistance was grouped into four categories: I_{90} =1.0, sensitive, I_{90} =1.01-10.0, slight resistance, I_{90}=10.01-100.0, moderate resistance, and $I_{90} \geq 100.0$, high resistance [17].

4.3.2.3 Survival rate

The stability of the AM^R parasite line was evaluated by: (i) five drug-free passages (5DFPs), with infection of parasites from the 20th cycle into naïve mice; (ii) revival of parasites cryopreserved (CP) for 3 months; and (iii) drug-free serial passages (DFSPs) for 4 months as shown in Fig. 4.1b. Drug susceptibility tests were performed in the three setups to determine the new ED_{50} and ED_{90} values, and compared with values obtained for the 20th cycle of AM-DP [17]. Artemether-exposed (AM^R) and the wild-type (AM^S) isogenic strain were serially passaged after 20 cycles of drug pressure for 16 and 32 generations, which lasted for approximately 2 and 4 months, respectively. At each specific time point, these parasites were sub-passaged into further groups of mice and subjected to *in vivo* drug sensitivity studies (with a pre-determined dose) to test their responses to artemether, such that for AM^S and AM^R parasites, there would be both a treated group and a corresponding untreated group. Parasitaemia on Day 4 and Day 7 pi in the course of DFSPs was used to assess the growth rate for the AM^R parasites relative to their AM^S progenitor, and thus their fitness. The percentage loss of fitness of the mutant parasite line relative to the wild-type/parent strain was expressed using Eq. 5 [24]:

$$P_r = 100 - \left[\frac{Mean\ parasitemia\ mutant}{Mean\ parasitemia\ wildtype}\right] \times 100 \qquad (4.5)$$

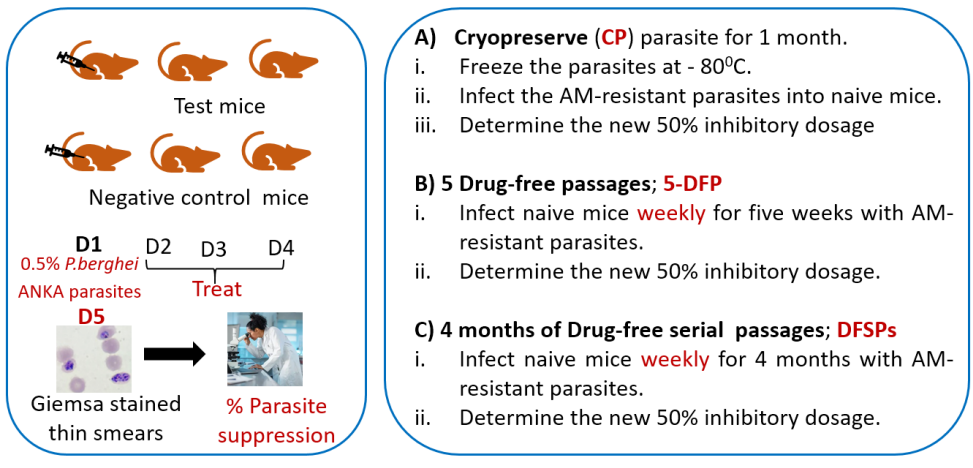

(a) (b)

Fig.4.1. Evaluation of: a) artemether-resistance, and b) survival rate.

4.4 Experimental results

4.4.1 ED_{50} and ED_{90} for the parent strain

P_p values for *P. berghei* ANKA against artemether were 78.87%, 56.5%, and 54.70% at drug doses of 2.5, 1.25, and 0.625 mg/kg body weight, respectively. The ED_{50} and ED_{90} were 0.61 and 3.43 mg/kg/day, respectively as shown in Fig. 4.2a.

4.4.2 Artemether resistance

After 270 days of continuous AM-DP dose, the artemether-resistant parasite line tolerated a drug dose of > 80 mg/kg body weight respectively as shown in Fig. 4.2b. ED_{50} and ED_{90} increased to 5.061 and 46.12 mg/kg/day, and 12.0 and 73.6 mg/kg/day after 120 days and 270 days, respectively as shown in Fig. 4.3a. I_{50} and I_{90} were 8.20 and 13.45, and 19.67 and 21.45 after 120 days and 270 days respectively as shown in Fig. 4.3b.

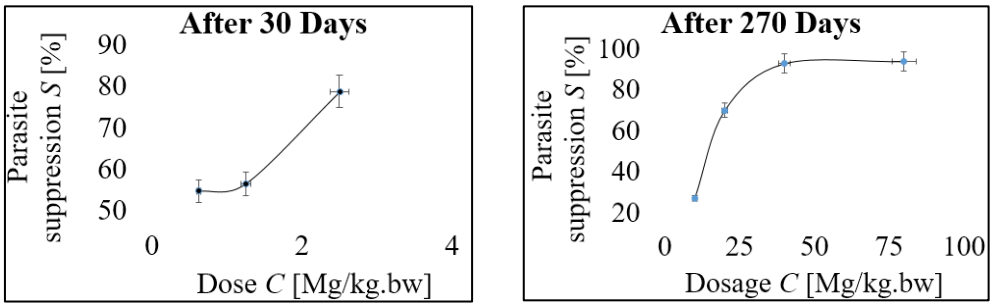

(a) (b)

Fig.4.2. Changes in chemosuppression (%): a) After 30 days, and b) 270 days of artemether resistance.

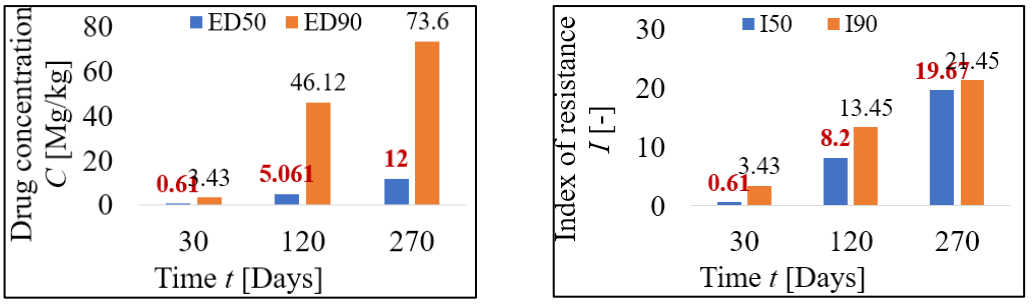

(a) (b)

Fig.4.3. Changes of artemether resistance over 270 days: a) 50% & 90% effective inhibitory dosages, and b) Index of resistance-50 & 90.

4.4.3 Survival rate of artemether resistance

Drug susceptibility tests using the 4-day suppressive test confirmed that the drug-exposed parasites did not lose their resistance after 5DFP, 3 months of CP, or DFSPs after 4 months. Overall, the AM^R line retained resistance, yielding ED_{50} and ED_{90} with 5DFP values of 23.89 and 52.36 mg/kg body weight, respectively; 3-month CP values of 17.91 and 37.02 mg/kg body weight, respectively; and DFSPs values of 19.12 and 42.16 mg/kg body weight, respectively as shown Fig. 4.4a. For I_{50} and I_{90}, 5DFP values were 39.16 and 15.27, respectively; 3-month CP values were 29.36 and 10.79, respectively; and DFSPs values were 31.34 and 12.29, respectively as shown in Fig. 4.4b. Parallel serial passaging of AM^R and AM^S parasites showed that the AM^R line had a significantly slower growth rate ($P<0.05$) over 2 months of passages, with mean parasitemia of 16.0% ± 1.80 compared with 33.98% ± 4.81 for the wild-type parasite at Day 4 pi and 18.78% ± 1.54 compared with 39.50% ± 5.02 for the wild-type parasite at Day 7 pi as shown in Fig. 4.5a. The AM^R strain showed a significantly lower ($P < 0.05$) growth rate over 4 months of DFSPs, with mean parasitemia of 18.18% ± 2.10 compared with 33.77% ± 3.98 for the wild-type parasite at Day 4 pi; and mean parasitemia of 24.70% ± 3.60 compared with 37.66% ± 3.68 for the wild-type parasite at Day 7 pi (Fig. 4.5b). The differences in parasitemia on D7 pi demonstrate that artemether resistance leads to a 34.41% loss of fitness which translates to a survival rate of 65.59%.

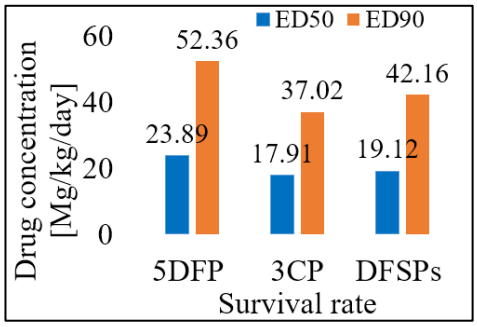

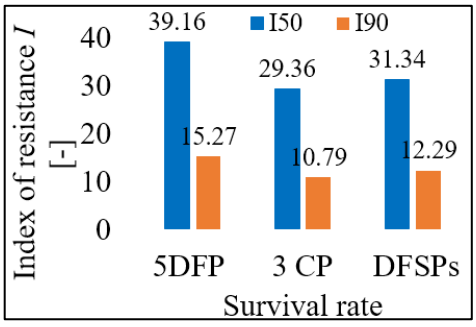

(a) (b)

Fig. 4.3. Survival rate of artemether resistance: a) 50% & 90% effective inhibitory dosages, and b) Index of resistance-50 & 90.

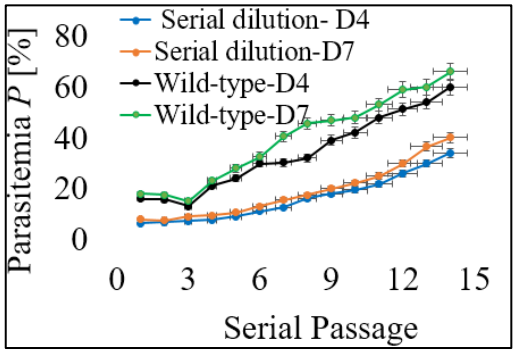

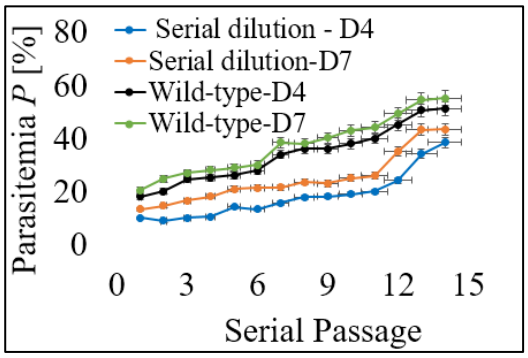

(a) (b)

Fig.4.5. Growth patterns for artemether resistant (AM^R) *Plasmodium berghei* ANKA parasites between Day 4 (D4) and Day 7 (D7) post-infection in the absence of drug: a) After 2 months and b) After 4 months.

4.5 Discussion

The rapid and unexpected upsurge of resistance to artemisinin derivatives and other antimalarial drugs can comprehensively thwart advances in combating and controlling malaria [2]. The greatest concern is the increasing global resistance of *P. falciparum* to partner drugs used in combination with the artemisinin derivatives. More pronounced gametocyte circulation carrying resistant genes, recrudescence, increased transmission, drug response, increased clinical cases and the level of reservoirs of resistant isolates

compared with sensitive isolates contribute to increased cases of emergence and spread of antimalarial drug resistance [8]. To understand resistance to the artemisinin drugs, this study used artemether to select resistant isolates in a mouse model, using methods adopted in other studies such as the development of pyronaridine resistance [17].

After 10 and 20 cycles of continuous AM-DP doses, performed for 9 months, the selected resistant parasite line tolerated a dose of >20 and 80 mg/kg body weight, respectively. ED_{50} and ED_{90} increased from 0.61 and 3.43 mg/kg/day (parent strain) to 12.0 and 73.6 mg/kg/day after 270 days. After 5DFP, the resistant line was stable with ED_{50} of 23.89 mg/kg/day, compared with 0.61 mg/kg/day for susceptible parasites, which confirmed the development of a moderate *P. berghei* AM^R phenotype. These results are consistent with a previous study that selected stable *P. chabaudi* artemisinin and artesunate-resistant phenotypes [19]. However, separate research selected unstable *P. berghei* ANKA artemether-resistant phenotypes through continuous exposure to single high-doses [18].

Alterations that render an organism resistant to a drug are likely associated with a loss of fitness [25]. To further the knowledge of the impact of resistance on parasite fitness, generated AM^R parasites were passaged serially (DFSPs) for 2 and 4 months. The parasite growth rate was almost two-fold faster for AM^S parasites by Day 7 pi after 4 months of DFSPs, with a 34.41% fitness cost for the AM^R parasite line. Deviations in resistance stability and the fitness cost of resistance may occur due to differences in resistance mechanisms for different drugs due to epigenetic modification [26] or genetic factors associated with the fitness cost [27]. Other mechanisms of sustaining resistance in artificially induced resistant parasites could also be involved, including transient changes in gene expression, which may account for the loss of resistance after cryopreservation of parasites as observed by Hunt et al. The fact that the revived parasites showed moderately high I_{50} (31.34) after DFSPs confirmed the stability of this artificially generated AM^R line.

A key determinant of the time course taken for a resistant variant to spread extensively to weaken the clinical worth of a drug is the forte of resistance selection. For instance, even minor changes in the relative fitness cost of wild-type and drug-resistant pathogens can modify the therapeutic lifespan of a drug for decades [28]. Notably, whether or not the mechanisms that underlie resistance of different artemisinin

derivatives will be similar is arguable [15], [29]. Using murine malaria parasites could provide critical information on the resistance mechanisms to artemether and allied artemisinin derivatives. Importantly, reports have shown that the use of lumefantrine + artemether (Coartem) selected for two haplotypes at 86Y-184Y-1246Y and 86Y-184F-1246D of pfmdr1, a gene associated with changes in susceptibility to chloroquine [3]. Moreover, *Pf*ATP6, A623E, and S769N substitutions have been shown to contribute to *in-vitro* artemether resistance [8]. I*n-vitro* and *in-vivo* studies have shown that much resistance to artemisinins arises in parasites with gene mutations in the pfK13 propeller region, *Pf*ubp-1, *Pf*ATPase6, and amplification of copy numbers of *Pf*mdr1 and *Pf*CRT. Furthermore, a recent *in vitro* study has revealed that inserting a K13 mutant gene in sensitive parasites reduces artemisinin susceptibility [30].

4.6 Summary

Artemether resistance and survival rate were evaluated using *Plasmodium berghei* ANKA parasites in mice. The results show that:

i. Artemether resistance is moderately stable, (I_{90} = 15.27, 10.79, and 12.29).
ii. The survival rate is 65.59%.

References

[1] N. Noreen, A. Ullah, S. M. Salman, Y. Mabkhot, A. Alsayari, and S. L. Badshah, "New insights into the spread of resistance to artemisinin and its analogues," Dec. 01, 2021, *Elsevier Ltd*.

[2] M. Dhorda, C. Amaratunga, and A. M. Dondorp, "Artemisinin and multidrug-resistant Plasmodium falciparum - a threat for malaria control and elimination," Oct. 01, 2021, *NLM (Medline)*.

[3] C. Sisowath *et al.*, "The role of pfmdr1 in Plasmodium falciparum tolerance to artemether-lumefantrine in Africa," *Tropical Medicine and International Health*, vol. 12, no. 6, pp. 736–742, Jun. 2007.

[4] S. Takala-Harrison and M. K. Laufer, "Antimalarial drug resistance in Africa: Key lessons for the future," *Ann N Y Acad Sci*, vol. 1342, no. 1, pp. 62–67, Apr. 2015.

[5] S. K. Pandey, U. Anand, W. A. Siddiqui, and R. Tripathi, "Drug Development Strategies for Malaria: With the Hope for New Antimalarial Drug Discovery—An Update," *Adv Med*, vol. 2023, pp. 1–10, Mar. 2023.

[6] M. Makanga and S. Krudsood, "The clinical efficacy of artemether/lumefantrine (Coartem®)," *Malar J*, vol. 8, no. SUPPL. 1, 2009.

[7] R. M. Fairhurst and A. M. Dondorp, " Artemisinin-Resistant Plasmodium falciparum Malaria ," *Microbiol Spectr*, vol. 4, no. 3, May 2016.

[8] F. A. Siddiqui, X. Liang, and L. Cui, "*Plasmodium falciparum* resistance to ACTs: Emergence, mechanisms, and outlook," *Int J Parasitol Drugs Drug Resist*, vol. 16, pp. 102–118, Aug. 2021.

[9] C. J. Woodrow and N. J. White, "The clinical impact of artemisinin resistance in Southeast Asia and the potential for future spread," Jan. 01, 2017, *Oxford University Press*.

[10] L. M. Montenegro, B. de las Salas, A. T. Neal, A. Tobon-Castaño, R. M. Fairhurst, and T. M. Lopera-Mesa, "State of artemisinin and partner drug susceptibility in plasmodium falciparum clinical isolates from Colombia," *American Journal of Tropical Medicine and Hygiene*, vol. 104, no. 1, pp. 263–270, Jan. 20218.

[11] H. C. Slater, J. T. Griffin, A. C. Ghani, and L. C. Okell, "Assessing the potential impact of artemisinin and partner drug resistance in sub-Saharan Africa," *Malar J*, vol. 15, no. 1, Jan. 2016.

[12] A. Uwimana *et al.*, "Association of Plasmodium falciparum kelch13 R561H genotypes with delayed parasite clearance in Rwanda: an open-label, single-arm, multicentre, therapeutic efficacy study," *Lancet Infect Dis*, vol. 21, no. 8, pp. 1120–1128, Aug. 2021.

[13] M. P. Kyaw *et al.*, "Reduced Susceptibility of Plasmodium falciparum to Artesunate in Southern Myanmar," *PLoS One*, vol. 8, no. 3, Mar. 2013.

[14] M. Ikeda *et al.*, "Artemisinin-resistant plasmodium falciparum with high survival rates, Uganda, 2014-2016," *Emerg Infect Dis*, vol. 24, no. 4, pp. 718–726, Apr. 2018.

[15] J. M.-R. Carlton, K. Hayton, P. V. L. Cravo, and D. Walliker, "Of mice and malaria mutants: unraveling the genetics of drug resistance using rodent malaria models," 2001. [Online].

[16] D. M. Kiboi *et al.*, "Plasmodium berghei ANKA: Selection of resistance to piperaquine and lumefantrine in a mouse model," *Exp Parasitol*, vol. 122, no. 3, pp. 196–202, Jul. 2009.

[17] S. K. Kimani, J. K. Nganga, D. W. Kariuki, J. Kinyua, F. T. Kimani, and D. M. Kiboi, "*Plasmodium berghei* ANKA: Selection of pyronaridine resistance in mouse model," *African Journal of Biochemistry Research*, vol. 8, no. 6, pp. 111–117, Aug. 2014.

[18] S. H. Xiao, J. M. Yao, J. Utzinger, Y. Cai, J. Chollet, and M. Tanner, "Selection and reversal of Plasmodium berghei resistance in the mouse model following repeated high doses of artemether," *Parasitol Res*, vol. 92, no. 3, pp. 215–219, Feb. 2004.

[19] R. T. Eastman and D. A. Fidock, "Artemisinin-based combination therapies: A vital tool in efforts to eliminate malaria," 2009.

[20] M. J. Mackinnon and A. F. Read, "Virulence in malaria: An evolutionary viewpoint," Jun. 29, 2004, *Royal Society*.

[21] M. J. Mackinnon and A. F. Read, "Immunity promotes virulence evolution in a malaria model," *PLoS Biol*, vol. 2, no. 9, Sep. 2004.

[22] M. W. Waithera *et al.*, "Antimalarial activity assay of artesunate-3-chloro-4(4-chlorophenoxy) aniline *in vitro* and in mice models," *Parasitol Res*, vol. 122, no. 4, pp. 979–988, Apr. 2023.

[23] M. Wekesa Sifuna, M. Wambui, J. Kang'Ethe Nganga, D. Wainaina Kariuki, F. T. Kimani, and F. W. Muregi, "Antiplasmodial Activity Assay of 3-Chloro-4-(4-chlorophenoxy) Aniline Combinations with Artesunate or Chloroquine in Vitro and in a Mouse Model," *Biomed Res Int*, vol. 2019, 2019.

[24] F. W. Muregi, I. Ohta, U. Masato, H. Kino, and A. Ishih, "Resistance of a rodent malaria parasite to a thymidylate synthase inhibitor induces an apoptotic parasite death and imposes a huge cost of fitness," *PLoS One*, vol. 6, no. 6, 2011.

[25] P. Hunt *et al.*, "Gene encoding a deubiquitinating enzyme is mutated in artesunate- and chloroquine-resistant rodent malaria parasites," *Mol Microbiol*, vol. 65, no. 1, pp. 27–40, Jul. 2007.

[26] A. Bird, "Perceptions of epigenetics," May 24, 2007, *Nature Publishing Group*.

[27] D. K. Raj *et al.*, "Disruption of a Plasmodium falciparum multidrug resistance-associated protein (PfMRP) alters its fitness and transport of antimalarial drugs and glutathione," *Journal of Biological Chemistry*, vol. 284, no. 12, pp. 7687–7696,

[28] A. R. Wargo, S. Huijben, J. C. De Roode, J. Shepherd, and A. F. Read, "Competitive release and facilitation of drug-resistant parasites after therapeutic chemotherapy in a rodent malaria model," 2007. [Online].

[29] A. Afonso *et al.*, "Malaria parasites can develop stable resistance to artemisinin but lack mutations in candidate genes atp6 (encoding the sarcoplasmic and endoplasmic reticulum Ca2+ ATPase), tctp, mdr1, and cg10," *Antimicrob Agents Chemother*, vol. 50, no. 2, pp. 480–489, Feb. 2006.

[30] O. Miotto *et al.*, "Emergence of artemisinin-resistant *Plasmodium falciparum* with kelch13 C580Y mutations on the island of New Guinea," *PLoS Pathog*, vol. 16, no. 12, Dec. 2020.

CHAPTER 5

Quantification of *Plasmodium falciparum* Infected Red Blood Cells by Electrical Impedance Spectroscopy and Distribution of Relaxation Times (EIS-DRT)

5.0 Quantification of *Plasmodium falciparum* infected red blood cells by electrical impedance spectroscopy and distribution of relaxation times (EIS-DRT)

5.1 Research Motivation

Rapid and accurate early-stage malaria diagnosis techniques are essential to guarantee appropriate and timely initiation of treatment interventions [1]. Conventional light microscopy can quantify *Plasmodium*-infected red blood cells (iRBCs) [2] but the procedure is time-consuming [3]. In addition, the need to use Giemsa-stained peripheral thick or thin blood smears requires high technical expertise to reduce false negative findings during routine clinical practices [4]. Alternative malaria diagnostic methods such as rapid diagnostic tests, calorimetric aptamer sensors, and electrochemical and immuno biosensors cannot quantify parasitemia because they detect biomarkers of malaria parasites such as *P. falciparum* histidine-rich protein 2 (HRP-2), *P. falciparum* lactate dehydrogenase (LDH), and *P. vivax* LDH antigens instead of parasites present [5], [6]. In addition, present-day *in vitro* drug assay protocols, such as the radio-labeled hypoxanthine-based technique used to quantify parasitemia, especially in sub-Saharan Africa's resource-limited malaria-endemic regions require many sample preparation steps and complex equipment, hence unreliable results.

Recently, a label-free electrical impedance spectroscopy (EIS) technique in which a small amplitude current signal is applied to a test sample, and the impedance response is measured over a wide range of frequencies [7], [8] has attracted much interest in biomedical research. EIS has been applied to monitor blood thrombus in cardiopulmonary bypass [9], quantify albumin and γ-globulin in solution [10], and characterize colorectal tumor cells based on their biophysical phenotypes [11]. In addition, EIS has been used to study the dielectric properties of nucleated RBCs (nRBCs) collected from bullfrogs [12], and in the quantification of living single yeast cells using an empirical model in mixtures of different volume fractions of living and dead cells [13].

In malaria research, Du et al distinguished single RBCs infected with ring stages of *P. falciparum* from uninfected RBCs suspended in 0.2 % bovine serum albumin-phosphate buffered saline solution at 2 MHz using a microfluidic cytometry EIS-based device [14] but no quantification of parasitemia was done. In another study, Ribaut et al

monitored the physiological changes of *P. falciparum* iRBCs immobilized on gold electrodes between a frequency range of 50 kHz to 100 MHz. To identify the biochemical changes associated with developing malaria parasites, a complex equivalent circuit model (ECM) was used to interpret the impedance data [15].

One major challenge in EIS-based studies is that the impedance data difficult to interpret. In most cases, it is fitted to an ECM that requires a priori information about the electrical properties of the test samples. Sometimes several impedance spectra can fit in a single ECM leading to ambiguity [16], [17]. In the recent past, an easy-to-use distribution of relaxation time (DRT) model, has gained much attention as an alternative to ECM because of its high temporal resolution [18], [19]. The results are easily interpreted since they are displayed as peaks with distinct relaxation time constants associated with separate polarization processes. Currently, two DRT analysis methods have been proposed: 1) standard DRT (sDRT) that requires pre-processing of the measured impedance spectra by modeling it in the frequency domain and identifying the model parameters by least-square fitting, followed by reduction of the measured spectra by subtracting the ohmic, inductive, and capacitive effects, and 2) generalized DRT (gDRT); measure impedance spectra, DRT calculation, and peak analysis respectively [19]. Previously, gDRT has been used to analyze impedance data in studies of lithium-ion batteries, vanadium redox flow batteries, and double-layer capacitors [19] and lung, kidney, and spleen tissues obtained from Winstar rats [20] In contrast, the sDRT has been used to analyze the impedance spectra of epithelial cell monolayers obtained from rat liver [21].

This study quantified *P. falciparum* iRBCs obtained from *in vitro* cultures by injecting 0.1mA current at a frequency range of 0.1-100 MHz by EIS-DRT method. Volume fractions (Ψ) of nucleated chicken (nRBCs) in un-nucleated porcine (uRBCs) were used for comparison analysis. The technique is envisioned as providing a rapid label-free platform for improved malaria diagnosis or alternative antimalarial drug screening protocol.

5.2 Experiment

5.2.1 Design and fabrication of Lab-on-CD prototype device

Fig.5.1 shows the Lab-on-compact disc (CD) device composed of a printed circuit board (PCB)-shaped double layer of radius r =100mm with 8 subminiature assembly (SMA) electrode (fixed and flexible) sensors fixed at the top. The bottom consists of an embedded 12-bit impedance analyzer controlled by a 32-bit advanced RISC (reduced instruction set computer) machine (ARM) microcontroller (Arduino Nano 33 IoT) which controls impedance measurement via an inter-integrated circuit (I2C) communication protocol. The 12-bit impedance analyzer is connected to two Analog multiplexers (MUX); 1:4 MUX (ADG1409) for amplification of the signal and 1:8 MUX (ADG1407) to control electrode switching. Fig.5.2 shows the fabricated device. The source of power for the device is a dual direct current regulator 5 VDC power bank.

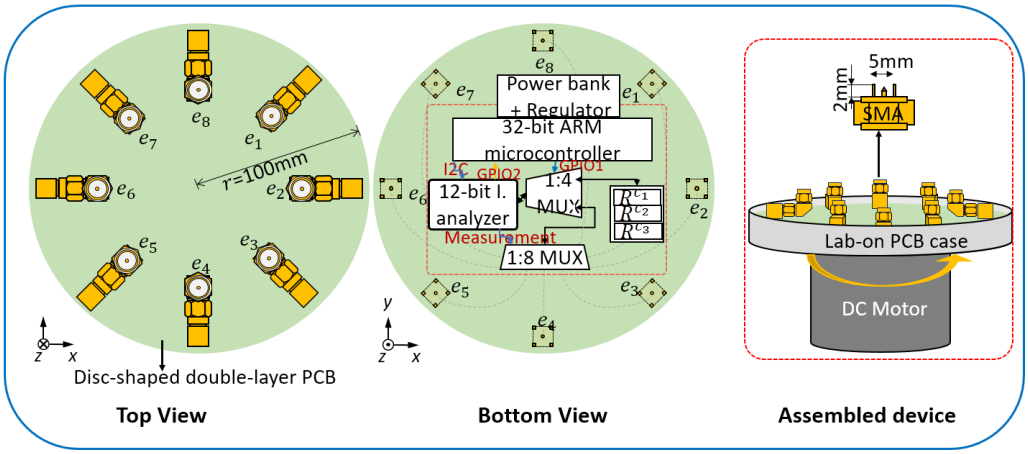

Fig.5.1. Design of the Lab-on-CD prototype device.

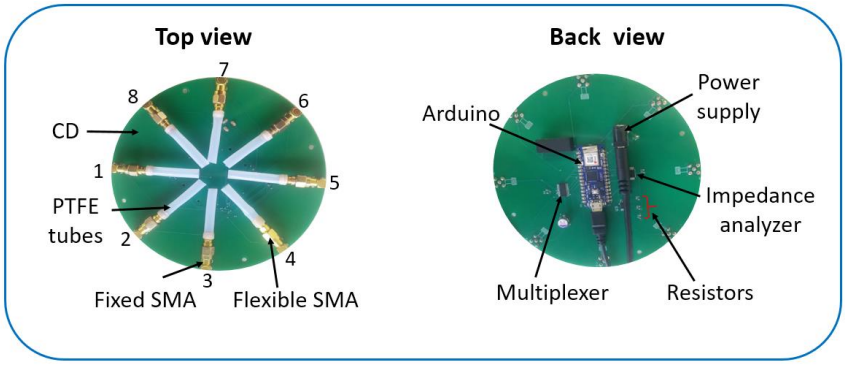

Fig.5.2. Fabricated Lab-on-CD prototype device.

5.2.3 Experimental setup

A sample holding cuvette of dimensions w×l×h = 2 mm × 12 mm × 45 mm comprising of two-platinum electrodes of h = 20 mm was connected to a conventional impedance analyzer, (IM 7581, Hioki E.E. Corporation Japan) via a test clip fixture (16092A; Keysight Technologies Co., Ltd., CA, USA) by coaxial cables. A laptop was used to control the impedance analyzer and process the data [10] as shown in Fig.5.3a. Polytetrafluoroethylene (PTFE) tubes of dimensions h = 30mm and diameter d =5mm were used for impedance measurement in the Lab-on-CD prototype device as shown in Fig.5.3b.

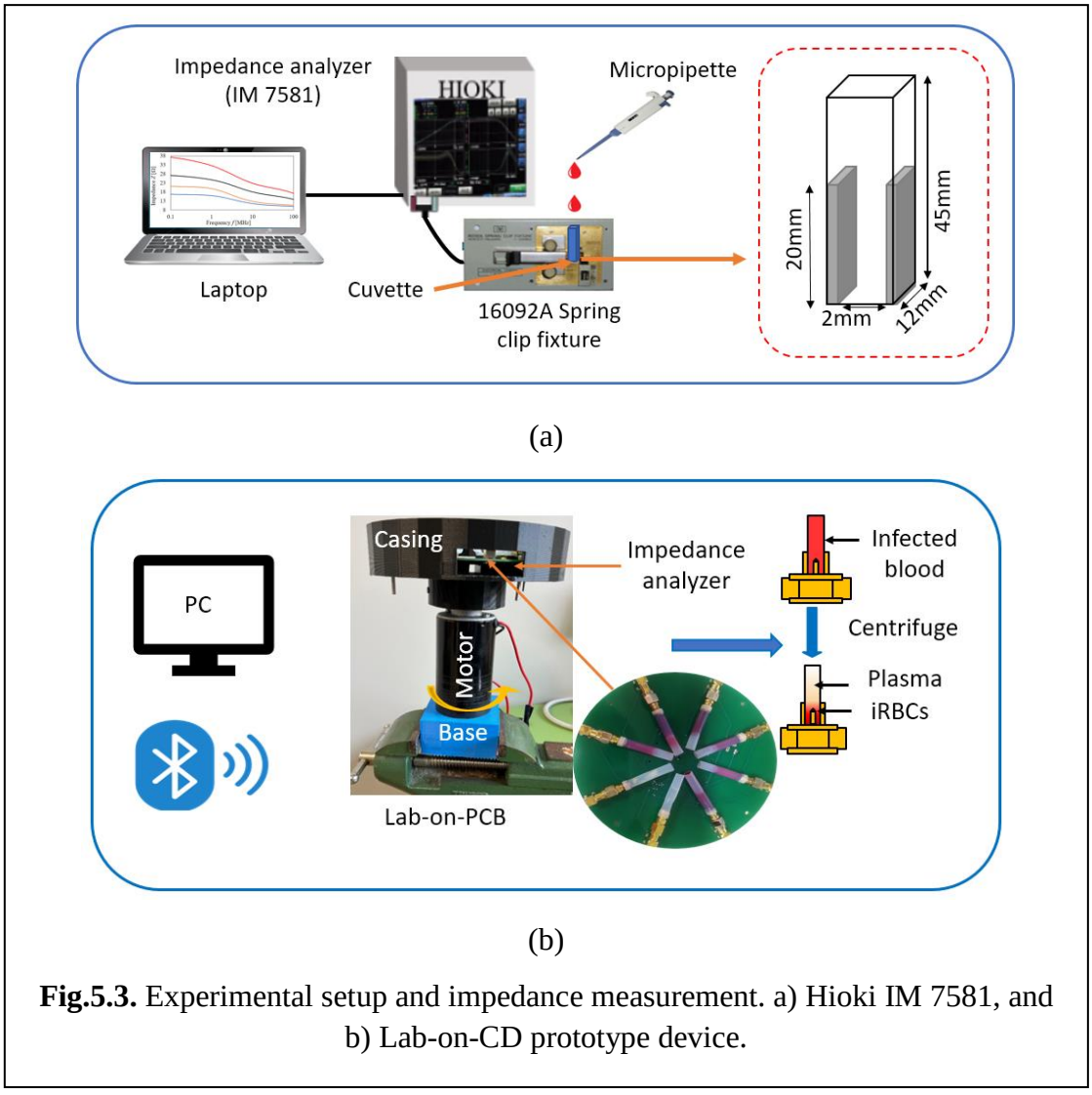

Fig.5.3. Experimental setup and impedance measurement. a) Hioki IM 7581, and b) Lab-on-CD prototype device.

5.2.4 Experimental methods

5.2.4.1 Preparation of *P. falciparum*-infected RBCs

This study was approved by the Bioethics Committee, Chiba University (authorization number: 3244) for clinical research with human blood samples. Human erythrocytes (A^+ blood type) and serum were obtained from the Japanese Red Cross Society (authorization number: 31J0050). *P. falciparum* 3D7 infected RBCs *in vitro* cultures consisting of mixtures of rings, trophozoites, and schizonts at 3.0 % hematocrit were prepared for microscopic observation. The parasitemia P (%) was determined on Giemsa-stained thin blood smears using Eq. 5.1 [22].

$$\mathrm{P}\ (\%) = \frac{T_{iRBCs}}{T_{RBCs}} \times 100 \tag{5.1}$$

P is percentage parasitemia, T_{iRBCs} is total number of infected red blood cells, and TiRBCs is total number of red blood cells.

The samples were centrifuged at 2,000 rpm for 15 minutes at room temperature (25^o). The supernatant was aspirated off to remove the effect of conductive external culture media including human serum. The buffy coat was also discarded and the packed RBCs resuspended in a 50 mM sucrose solution. Following a micro-centrifuge protocol (Model 3300; Kubota Corporation, Tokyo, Japan), the samples were adjusted to 3.0 % hematocrit.

5.2.4.2 Preparation of volume fractions of nucleated RBCs

Nucleated (nRBCs) and un-nucleated (uRBCs) were obtained from chicken and porcine blood respectively. The blood samples were aseptically drawn from the respective animals in the slaughterhouse (Shibaura Zouki, Japan) into tri-sodium citrate anticoagulated vessels (blood: tri-sodium citrate at a ratio of 9:1 and transported refrigerated to the laboratory [9]. For each type of blood, 15 mL was centrifuged as previously described. The supernatant (plasma and buffy coat) was aspirated off and packed RBCs were washed twice by resuspending in 3 mL of 50 mM sucrose solution. Following the previously stated microcentrifuge protocol, the hematocrit was adjusted to 40% and 50% using 50 mM sucrose solution.

To quantify the volume fractions (Ψ) of nRBCs, five blood samples were prepared at 35% hematocrit by adding (0.0, 0.2, 0.4, 0.6, and 0.8) mL nRBCs into separate test tubes and topping up the volume to 1 mL using uRBCs.

5.2.5 Experimental conditions

The impedance analyzer was initially calibrated using an open and 2 short loads following the manufacturer's protocol and 500 µL of blood samples (that completely covered the electrodes) was then pipetted into a cuvette one at a time. The impedance analyzer was prompted to inject a 0.1 mA constant stimulation current signal at a frequency range of 0.1 to 100 MHz. The electrical impedance parameters, complex impedance (Z), phase angle (θ), real (Z'), and imaginary (Z'') components of impedance were measured for each sample at 201 discrete frequency points evenly distributed on a logarithmic scale. On completion of the measurement, the blood was mixed and measured again and average values were used for impedance calculations. The frequency-based complex impedance of blood (Z_{blood}), and θ is given by Eqs 5.2 and 5.3.

$$Z_{blood}(f) = \frac{V}{I}[\cos\theta + j\sin\theta] \tag{5.2}$$

$$\theta = arctan\frac{Z''}{Z'} \tag{5.3}$$

V is voltage, I is current, and j is an imaginary unit.

Z_{blood} is also expressed in terms of Z' and Z'' given by Eqs 5.4 and 5.5, which provide Nyquist plots for further data analysis and interpretation, thus;

$$Z'(f) = Z_{blood}\ cos\theta \tag{5.4}$$

$$Z''(f) = Z_{blood}\ sin\theta \tag{5.5}$$

5.2.6. DRT analysis of impedance data

The measured frequency-dependent impedance (Z_{blood}) was transformed into the time domain using Eqs. 5.6 to 5.8 [20].

$$Z_{blood}(\omega) = R_{\infty} + \int_{-\infty}^{\infty}\frac{\gamma(ln\tau)}{1+j\omega\tau)}d(ln\tau) \tag{5.6}$$

γ (lnτ) is a function of the relaxation time distribution, τ is relaxation time and ω is angular frequency. Based on a regularized regression method, γ(lnτ) refers to the sum of Dirac distributions (δ(lnτ)) centered at N characteristic times t_1, t_2, . . . …t_N and it is given by Eq. 5.7.

$$\gamma(ln\tau) = \sum_{n=1}^{N} x_n \, \delta(ln\tau - ln\tau_n) \quad (5.7)$$

x_n is the amplitude of an n-th function centered at its corresponding τ_n. Combining Eqs. 5.6 and 5.7, the impedance spectra DRT (Z_{DRT}) is modeled by Eq.5. 8.

$$Z_{DRT}(\omega) = R_\infty + \sum_{n=1}^{N} x_n \int_{-\infty}^{\infty} \frac{\gamma(ln\tau)}{1+j\omega\tau)} d(ln\tau) \quad (5.8)$$

SPYDER (Python 10.3.9) algorithm was used to transform the Z_{blood} to the time domain. To facilitate an easy comparison of the impedance spectra and DRT plots, the relaxation times (τ) were converted to frequency using Eq. 5.9.

$$f(\text{Hz}) = \left(\frac{1}{(2^*\pi^*tau)}\right) \quad (5.9)$$

The results were displayed as peaks with amplitude maxima (γ_{max}) which represent separate polarization processes [23]. The changes in γ_{max} for *P. falciparum* iRBCs and nRBCs were then correlated by linear regression.

5.3. Experimental Results

5.3.1 Impedance spectra for *P. falciparum* iRBCs using Hioki IM 7581

Fig. 5.4 shows the impedance characteristics for *P. falciparum* iRBCs. Fig. 5.4a shows changes in impedance against frequency demonstrating dielectric relaxation phenomena at around 2 MHz. The magnitude decreases gradually with the increase in parasitemia. Fig. 5.4b shows the change in θ against frequency where the θ decreases with an increase in P. Generally, the decrease in phase angle is small from the low to the high frequency. Fig. 5.4c shows a Nyquist plot where the Z' impedance component decreases with the increase in parasitemia. Fig. 5.5 shows the changes in Z, Fig. 5.5a, and Z'', Fig. 5.5b components of complex impedance that characterize membrane changes following the invasion of the malaria parasites. The current starts to penetrate the plasma membrane and enters the cytoplasm as demonstrated by the dielectric relaxation phenomena in Fig. 5.5a. Fig. 5.5c shows the changes in Z' and Z'' at 2 MHz where both Z' and Z'' drop gradually with an increase in the percentage of parasitemia.

Fig. 5.6a shows the variations of the relaxation time distribution (γ) with *P*. The DRT plot has three peaks: I, II, and III. Peak III, with a relaxation frequency of 1.6 ×107 Hz, represents the impedance changes in the RBCs' cytoplasm due to biochemical

modifications caused by *P. falciparum* invasion [15]. Therefore, it was selected for further data analysis. The uninfected RBCs display the highest γ_{max} value of 12.1 Ω. In contrast, the *P. falciparum* iRBCs showed slightly lower γ_{max} of 11.7Ω, 11.0 Ω, and 9.9 Ω with an increase in parasitemia from 4.47%, 6.49%, and 10.84% respectively, a relationship modeled by γ_{max} = - 0.2037*P*+ 12.298 (R^2 = 0.94) as shown in Fig. 5.6b.

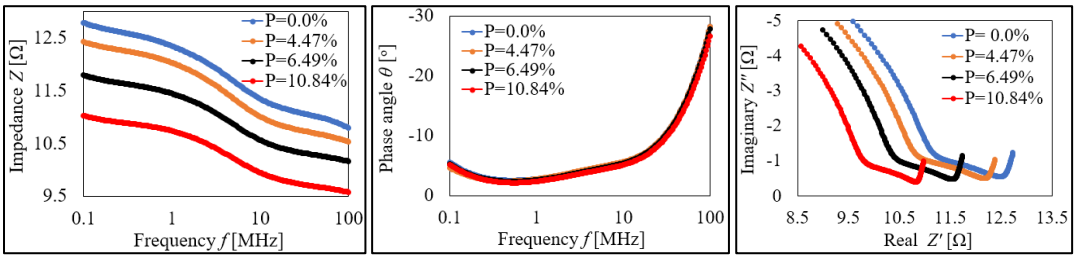

(a) (b) (c)

Fig. 5.4. Impedance characteristics for *P.falciparum* iRBCs at varying parasitemia, *P* across increasing frequency: (a) change in impedance amplitude, *Z* (b) change in phase angle θ, and (c) the relationship between real (Z') and imaginary (Z'') components of complex impedance.

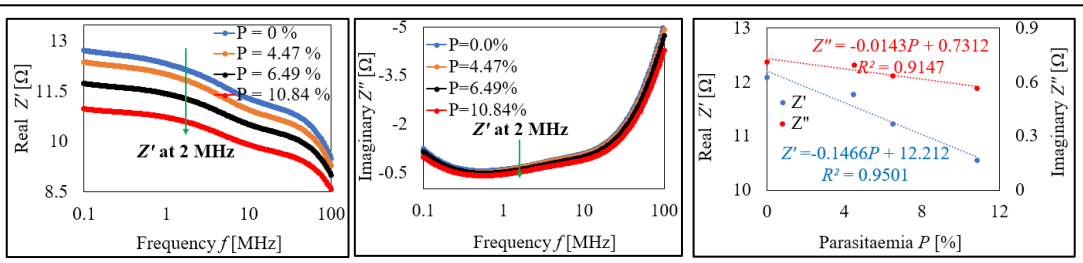

(a) (b) (c)

Fig. 5.5. Impedance characteristics for *P.falciparum* iRBCs at varying parasitemia, *P* across increasing frequency: (a) change in real (Z'), (b) change in imaginary (Z'') components of complex impedance, and (c) Z' and Z'' components of complex impedance at 2 MHz that characterize changes in the RBC's plasma membrane following the invasion of malaria parasites.

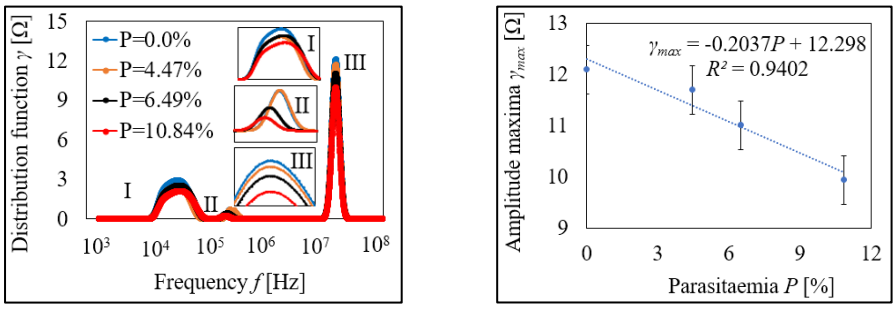

(a) (b)

Fig. 5.6. Relaxation time distribution (γ) for *P.falciparum* iRBCs: (a) variations of the distribution function (γ) with the increase in parasitemia, *P*, inset are enlarged peaks I, II & III respectively, and (b) the changes in amplitude maxima (γ_{max}) with the increase in *P* at a relaxation frequency of 1.6 $\times 10^7$ Hz.

5.3.2 Impedance spectra for *P. falciparum* iRBCs using Lab-on-CD prototype device

Fig. 5.7 shows the impedance characteristics for *P. falciparum* iRBCs at parasitemia *P*, 0% to 2.55% at a frequency range between 10-100 kHz. The results demonstrate consistency with the results obtained from the Hioki IM 7581 impedance analyzer where the Z, θ and Z' decrease gradually with the increase in P; $P = 1.55\% > P = 2.55\%$ as shown in Fig. 5.7a, b and c respectively.

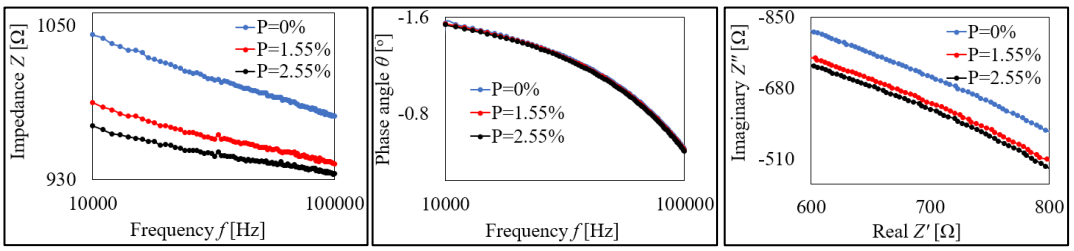

(a) (b) (c)

Fig. 5.7. Impedance characteristics for *P.falciparum* iRBCs at varying parasitemia, *P* across increasing frequency: (a) change in impedance amplitude, *Z* (b) change in phase angle θ, and (c) the relationship between real (Z') and imaginary (Z'') components of complex impedance.

5.3.3. Impedance spectra for nucleated and un-nucleated RBCs

Fig. 5.8 shows impedance characteristics for nRBCs and uRBCs at 40% and 50% *Hct*. The impedance of nRBCs was higher than that of uRBCs as demonstrated in Fig. 5.8a. The change in impedance decreases gradually at a frequency greater than 5 MHz and then slowly up to 100 MHz. Fig. 5.8b shows that the phase angle in both nRBCs and uRBCs at 50% *Hct* is slightly higher than that at 40% *Hct*. Fig. 5.8c is a Nyquist plot which shows that the resistance in uRBCs is lower than that of the nRBCs and increases with the increase in *Hct*. The nRBCs (chicken) are oval and larger than the uRBCs (porcine) which are round [24]. The larger size makes the nRBCs more capacitive than the uRBCs, resulting in higher resistance for nRBCs than the uRBCs.

The DRT plot in Fig. 5.9a displays three peaks; I, II, and III. Peak III exhibits γ_{max} at f = 1.6 ×10^7 Hz. The nRBCs exhibited higher γ_{max} of 28.2±2.7 Ω and 33.6±2.7 Ω compared to 14.6±0.9 Ω and 16.5±0.9 Ω for uRBCs at 40% *Hct* and 50% *Hct* respectively which is associated with the morphological differences between the two types of cells as shown in Fig. 5.9b. The presence of the nucleus forms an additional barrier to the flow of electrical current into the RBCs cytoplasm, which might explain the observed higher γ_{max} [21].

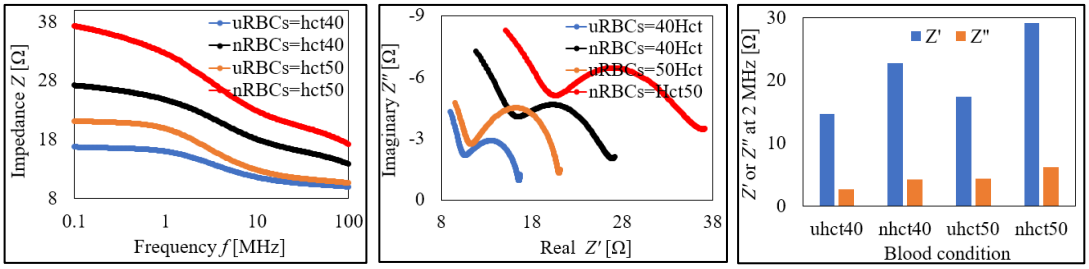

(a) (b) (c)

Fig. 5.8. Impedance characteristics for un-nucleated (uRBCs) and nucleated (nRBCs) at 40% and 50% hematocrit: (a) change in impedance amplitude, Z (b) the relationship between real (Z') and imaginary (Z'') components of complex impedance, and (c) real (Z') and imaginary (Z'') components of complex impedance at 2 MHz.

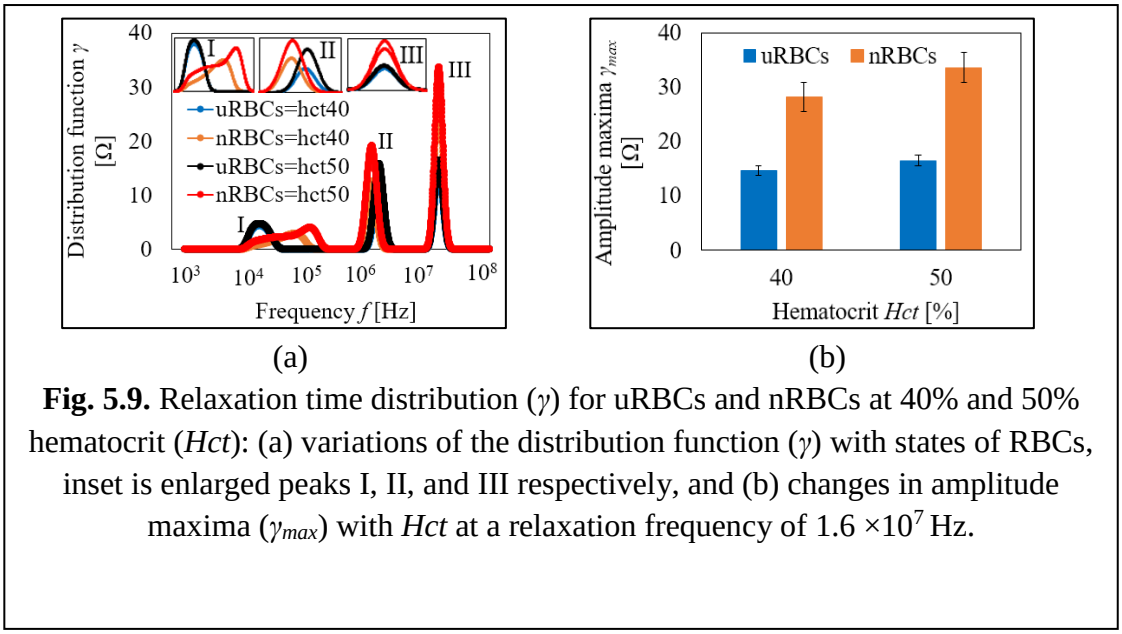

(a) (b)

Fig. 5.9. Relaxation time distribution (γ) for uRBCs and nRBCs at 40% and 50% hematocrit (*Hct*): (a) variations of the distribution function (γ) with states of RBCs, inset is enlarged peaks I, II, and III respectively, and (b) changes in amplitude maxima (γ_{max}) with *Hct* at a relaxation frequency of 1.6 $\times 10^7$ Hz.

5.3.4. Impedance spectra for volume fractions of nucleated RBCs

Fig. 5.10 shows impedance characteristics for volume fractions (Ψ) of nRBCs in uRBCs. In Fig. 5.10a, the impedance increases with the increase in Ψ of nRBCs from 0.0 to 0.8. The θ slightly increases with the rise in Ψ of nRBCs as shown in Fig. 10b.The resistance increases with the rise in Ψ of nRBCs as shown in the Nyquist plot in Fig. 10c. Fig. 11a shows changes in γ against the frequency, f with three peaks; I, II, and III. The γ_{max} for peak III is $f = 1.6\times10^7$ Hz. The Ψ (0.0, 0.2, 0.4, 0.6, and 0.8) positively correlate with the γ_{max} where the γ_{max} increase from 11.7±0.8 Ω, 12.7±0.8 Ω, 13.8±0.8 Ω, 15.0±0.8 Ω, and 15.9±0.8 Ω respectively, a relationship modeled by $\gamma_{max} = 5.35\ \Psi + 11.68$, ($R^2 = 0.99$) as shown in Fig. 11b.

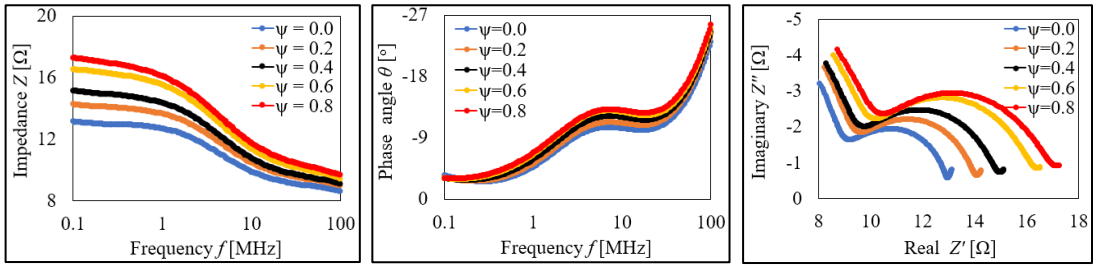

(a) (b) (c)

Fig. 5.10. Impedance characteristics for volume fractions (Ψ) of nRBCs in uRBCs across increasing frequency: (a) change in impedance amplitude, Z, (b) change in phase angle θ, and (c) the relationship between real (Z') and imaginary (Z'') components of complex impedance.

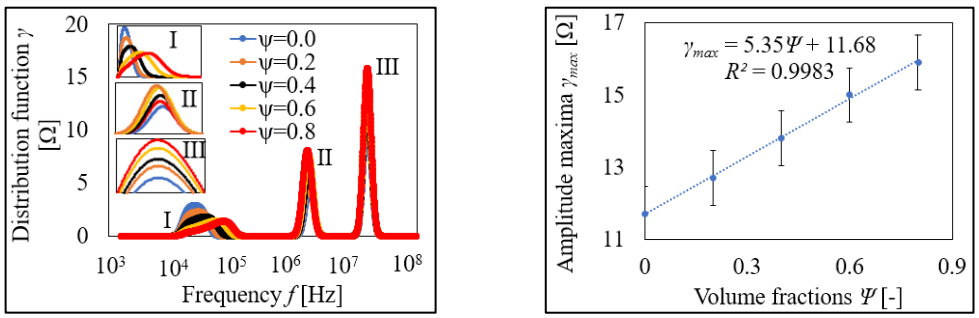

(a) (b)

Fig. 5.11. Relaxation time distribution (γ) for volume fractions (Ψ) of nRBCs in uRBCs: (a) variations of the distribution function (γ) with Ψ, inset are enlarged peaks I, II & III respectively, and (b) the changes in amplitude maxima (γ_{max}) with increasing Ψ at a relaxation frequency of 1.6 $\times 10^7$ Hz.

5.4. Discussion

5.4.1 Impedance spectra for *P. falciparum* iRBCs

In malaria infection, the parasite becomes metabolically active. It remodels the host's RBC plasma membrane and induces new permeation pathways to compensate for the high demand for essential nutrients. The new permeation pathways drastically increase the permeability of the parasite's plasma membrane to various extracellular low molecular weight solutes such as purines, isoleucine, and vitamin B5 which are critical for the parasite's growth and survival [25]. The observed drop in Z' and Z'' at 2 MHz is possibly due to the new permeation pathways which make the plasma membrane more conductive, lowering its capacity to absorb and store charge (capacitance). In addition, the parasite forms cystosomes which facilitate the endocytotic trafficking of hemoglobin from the host RBC cytoplasm into the parasitophorous vacuole where the parasite resides and into the digestive food vacuole. The hemoglobin is metabolized into heme and converted to less toxic hemozoin crystals that exit the food vacuole into the RBCs' cytoplasm [26]. Therefore, the increased heme concentration and extracellular flux of Na^+ from the parasite's cytoplasm into the RBCs cytoplasm largely contribute to the decrease in the cytoplasm resistance after 2 MHz as shown in Fig. 3a [27]. The reduction in γ_{max} as the parasitemia increases is consistent with a previous study which has demonstrated that RBCs exhibit maximum polarization and β-dispersion at the high frequency of around 2 MHz which allows the current to pass through the RBCs plasma membrane into the cytoplasm [15]. Moreover, the increased permeability of the RBC plasma membrane to the human host metabolites also accounts for the decrease in γ_{max} with an increase in parasitemia [21].

5.4.2 Impedance spectra for volume fractions of nucleated RBCs

The observed difference in impedance characteristics between nRBCs and uRBCs is associated with the morphological differences between the two types of cells. The nRBCs (chicken) are oval and larger (10.48 mm) than the uRBCs (porcine) which are round and smaller (5.85 mm) [24]. The larger size makes the nRBCs more capacitive than the uRBCs resulting in the higher resistance observed for nRBCs compared to uRBCs. Also, the presence of the nucleus forms an additional barrier to the flow of electrical current into the RBC cytoplasm which might explain the observed higher amplitude maxima.

The observed changes in impedance characteristics are consistent with a study by Xu et al, which evaluated the dielectric properties of nucleated RBCs obtained from bullfrogs at a frequency of 10 kHz to 110 MHz.

5.5. Summary

The current study proposes electrical impedance spectroscopy integrated with the distribution of relaxation times (EIS-DRT) for quantifying parasitemia (*P*). *Plasmodium falciparum* infected red blood cells (iRBCs) at increasing *P* (%), obtained from *in vitro* cultures were prepared for impedance measurements. The electrical impedance was measured using a conventional impedance analyzer; Hioki IM 7581 by injecting 0.1mA current at a frequency between 0.1-100 MHz. Volume fractions (Ψ) of nucleated chicken nRBCs in un-nucleated porcine uRBCs were used for comparison analysis. A Lab-on-compact disc (CD) impedance analyzer prototype device was used to validate the results of iRBCs by measuring the impedance at 10-100 kHz. The results show that the cells' impedance spectra have three DRT peaks: I, II, and III. Peak III with a relaxation frequency of 1.6×10^7 Hz represents the impedance changes in the RBCs' cytoplasm due to biochemical modifications caused by *P. falciparum* invasion or the presence of the nucleus and was selected for further analysis. The amplitude maxima (γ_{max}) for the iRBCs decreases from 11.7±0.5 Ω to 9.9±0.5 Ω with the rise in *P* from 4.47% to 10.84%, a relationship modeled by γ_{max} = -0. 2037*P*+12.298 (R^2 = 0.94). The impedance characteristics from the Lab-on-CD device show consistency with the results obtained from the Hioki IM 7581 where the impedance (*Z*), phase angle (θ), and real component of complex impedance (*Z'*) decrease gradually with the increase in parasitemia (*P*); *P* = 1.55% > *P* = 2.55%. The technique is envisioned as providing a rapid label-free platform for improved malaria diagnosis or alternative reliable antimalarial drug screening protocol.

References

[1] M. A. Saeed and A. Jabbara, "'Smart diagnosis' of parasitic diseases by use of smartphones," *J Clin Microbiol,* vol. 56, no. 1, Jan. 2018.

[2] O. O. Oyegoke *et al.*, "Malaria diagnostic methods with the elimination goal in view," Jul. 01, 2022, *Springer Science and Business Media Deutschland GmbH*.

[3] A. Mbanefo and N. Kumar, "Evaluation of malaria diagnostic methods as a key for successful control and elimination programs," Jun. 01, 2020, *MDPI AG*.

[4] W. O. Otambo *et al.*, "Health care provider practices in diagnosis and treatment of malaria in rural communities in Kisumu County, Kenya," *Malar J,* vol. 21, no. 1, Dec. 2022.

[5] K. V. Ragavan, S. Kumar, S. Swaraj, and S. Neethirajan, "Advances in biosensors and optical assays for diagnosis and detection of malaria," May 15, 2018, *Elsevier Ltd*.

[6] G. Dutta, "Electrochemical biosensors for rapid detection of malaria," Jan. 01, 2020, *KeAi Communications Co.*

[7] H. S. Magar, R. Y. A. Hassan, and A. Mulchandani, "Electrochemical impedance spectroscopy (Eis): Principles, construction, and biosensing applications," Oct. 01, 2021, *MDPI*.

[8] A. C. Lazanas and M. I. Prodromidis, "Electrochemical Impedance Spectroscopy─A Tutorial," Jun. 21, 2023, *American Chemical Society*.

[9] M. W. Sifuna *et al.*, "Connector sensors for permittivity-based thrombus monitoring in extracorporeal life support," *Journal of Artificial Organs*, vol. 24, no. 1, pp. 15–21, Mar. 2021.

[10] M. W. Sifuna, M. R. Baidillah, A. Sapkota, and M. Takei, "A Cole-Cole Dielectric Relaxation Analysis of Albumin and γ-Globulins for Protein Quantification by Electrical Impedance Spectroscopy," *Electroanalysis*, vol. 32, no. 5, pp. 1121–1129, May 2020.

[11] I. Turcan *et al.*, “Dielectrophoretic and electrical impedance differentiation of cancerous cells based on biophysical phenotype,” *Biosensors (Basel)*, vol. 11, no. 10, Oct. 2021.

[12] J. Xu, W. Xie, Y. Chen, L. Wang, and Q. Ma, “Dielectric properties of nucleated erythrocytes as simulated by the double spherical-shell model,” *Chinese Physics B*, vol. 29, no. 12, Dec. 2020.

[13] X. Liu, Y. Cui, T. Zhao, D. Kawashima, H. Obara, and M. Takei, “Quantitative Detection of Living Yeast Fraction from Mixed Living and Dead Cell Solution by Micro Electrical Impedance Spectroscopy,” *IEEE Access*, vol. 7, pp. 33970–33977, 2019.

[14] E. Du, S. Ha, M. Diez-Silva, M. Dao, S. Suresh, and A. P. Chandrakasan, “Electric impedance microflow cytometry for characterization of cell disease states,” *Lab Chip*, vol. 13, no. 19, pp. 3903–3909, Oct. 2013.

[15] C. Ribaut *et al.*, “Electrochemical impedance spectroscopy to study physiological changes affecting the red blood cell after invasion by malaria parasites,” *Biosens Bioelectron*, vol. 24, no. 8, pp. 2721–2725, Apr. 2009.

[16] H. Bao *et al.*, “Quantitative evaluation of burn injuries based on electrical impedance spectroscopy of blood with a seven-parameter equivalent circuit,” *Sensors*, vol. 21, no. 4, pp. 1–8, Feb. 2021.

[17] P. Jash, R. K. Parashar, C. Fontanesi, and P. C. Mondal, “The Importance of Electrical Impedance Spectroscopy and Equivalent Circuit Analysis on Nanoscale Molecular Electronic Devices,” Mar. 01, 2022, *John Wiley and Sons Inc*.

[18] B. A. Boukamp, “Distribution (function) of relaxation times, successor to complex nonlinear least squares analysis of electrochemical impedance spectroscopy?,” Oct. 01, 2020, *IOP Publishing Ltd*.

[19] M. A. Danzer, “Generalized distribution of relaxation times analysis for the characterization of impedance spectra,” *Batteries*, vol. 5, no. 3, Sep. 2019.

[20] R. G. Ramírez-Chavarría, C. Sánchez-Pérez, and D. Matatagui, “Analysis of Impedance Spectroscopy Measurements of Biological Tissue using the Distribution of Relaxation Times Method,” in *BIODEVICES 2017 - 10th International Conference on Biomedical Electronics and Devices, Proceedings; Part of 10th International Joint Conference on Biomedical Engineering Systems and Technologies, BIOSTEC 2017*, SciTePress, 2017, pp. 224–228.

[21] F. Shi and J. F. Kolb, “Enhanced resolution impedimetric analysis of cell responses from the distribution of relaxation times,” *Biosens Bioelectron*, vol. 157, Jun. 2020.

[22] M. W. Waithera *et al.*, “Antimalarial activity assay of artesunate-3-chloro-4(4-chlorophenoxy) aniline in vitro and in mice models,” *Parasitol Res*, vol. 122, no. 4, pp. 979–988, Apr. 2023.

[23] T. H. Wan, M. Saccoccio, C. Chen, and F. Ciucci, “Influence of the Discretization Methods on the Distribution of Relaxation Times Deconvolution: Implementing Radial Basis Functions with DRTtools,” *Electrochim Acta*, vol. 184, pp. 483–499, 2015.

[24] S. Sorapukdee and S. Narunatsopanon, “Comparative study on compositions and functional properties of porcine, chicken and duck blood,” *Korean J Food Sci Anim Resour*, vol. 37, no. 2, pp. 228–241, Apr. 2017.

[25] N. A. Counihan, J. K. Modak, and T. F. de Koning-Ward, “How Malaria Parasites Acquire Nutrients From Their Host,” Mar. 25, 2021, *Frontiers Media S.A.*

[26] L. Tilley, M. W. A. Dixon, and K. Kirk, “The Plasmodium falciparum-infected red blood cell,” 2011, *Elsevier Ltd*.

[27] K. Kirk, “Membrane Transport in the Malaria-Infected Erythrocyte,” 2001. [Online]. Available: http://physrev.physiology.org

CHAPTER 6

Research Summary

6.0 Research Summary

6.1 Summary

This thesis aims to develop early-stage malaria treatment and diagnosis by hybrid drugs and electrical impedance spectroscopy. This study has three originalities 1) the development of hybrid drugs: Artesunate 4-Chlorophenoxy aniline, 2) the evaluation of artemether resistance and survival rate, and 3) the quantification of parasitemia of *Plasmodium falciparum*-infected RBCs by EIS. The details are summarized as follows:

CHAPTER 1

This chapter introduces the contents of this thesis, which are early-stage malaria treatment and diagnosis by hybrid drugs & EIS. It also summarizes the challenges of conventional treatment methods and diagnosis techniques.

CHAPTER 2

This chapter gives a general overview of the three main topics of this thesis: Hybrid drugs, artemether resistance, and electrical impedance spectroscopy and distribution of relaxation time (EIS-DRT). Hybrid drugs are synthesized by combining two molecules with distinct mechanisms of action into one compound in a concept known as covalent biotherapy. Understanding the molecular mechanisms associated with artemether resistance is key in monitoring the emergence of resistance. The insights will guide approaches aimed at mitigating these occurrences. EIS is an analytical technique that applies a small amplitude signal to a biological sample, and the impedance response is measured over a wide frequency range. This technique has found many applications in the biomedical field. DRT analysis is an alternative technique for interpreting the impedance data from frequency to time domain with results displayed as peaks representing distinct polarization processes.

CHAPTER 3

This chapter presents the overview of hybrid drugs: artesunate 4-Chlorophenoxy aniline (ATSA) and its in silico absorption, distribution, metabolism, and toxicity (ADMET) profiles. ATSA was evaluated using *Plasmodium falciparum* and *P. berghei*

ANKA parasites *in vitro and in vivo* respectively. The results demonstrate that the ATSA the *in vitro* antiplasmodial activity is 11.47±1.3 ng/ml, 3D7 strain with a wide safety margin, selective index (SI) > 2000. The *in vivo* antimalarial chemosuppression is above 40%. ATSA has a high predicted intestinal absorption (HIA), > 95%, and a medium human ether-a-go-go-related gene (hERG) K^+ channel inhibition risk.

CHAPTER 4

This chapter presents artemether resistance and survival rate using *Plasmodium berghei* ANKA parasites. Artemether resistance is moderately stable: (I_{90} = 15.27, 10.79, and 12.29) and the survival rate is 65.59%.

CHAPTER 5

This chapter proposes electrical impedance spectroscopy and distribution of relaxation times (EIS-DRT) for quantifying parasitemia *P* (%) of *P.falciparum* infected red blood cells (iRBCs) obtained from *in vitro* cultures. The electrical impedance was measured using a conventional impedance analyzer; Hioki IM 7581 by injecting 0.1mA current at a frequency between 0.1-100 MHz. Volume fractions (Ψ) of nucleated chicken nRBCs in un-nucleated porcine uRBCs were used for comparison analysis. A Lab-on-compact disc (CD) impedance analyzer prototype device was used to validate the results from iRBCs by measuring the impedance at 10-100 kHz. The results show that the cells' impedance spectra have three DRT peaks: I, II, and III. Peak III with a relaxation frequency of 1.6×10^7 Hz represents the impedance changes in the RBCs' cytoplasm due to biochemical modifications caused by *P. falciparum* invasion or the presence of the nucleus and was selected for further analysis. The amplitude maxima (γ_{max}) for the iRBCs decreases from 11.7±0.5 Ω to 9.9±0.5 Ω with the rise in *P* from 4.47% to 10.84%, a relationship modeled by γ_{max} = -0. 2037*P*+12.298 (R^2 = 0.94). The impedance characteristics from the Lab-on-CD device show consistency with the results obtained from Hioki IM 7581 where the impedance (*Z*), phase angle (θ), and real component of complex impedance (*Z'*) decrease gradually with the increase in parasitemia (*P*); *P* = 1.55% > *P* = 2.55%. The technique is envisioned as providing a rapid label-free platform for improved malaria diagnosis or alternative reliable antimalarial drug screening protocol.

Acknowledgments

My extreme gratitude is to the mighty **GOD** for his mercies, goodness, and faithfulness.

My greatest appreciation goes to my family for their emotional support and prayers. Thank you for cheering me on! God bless you abundantly.

To my supervisor **Prof. Masahiro Takei**, thank you for introducing me to electrical impedance spectroscopy research. I am grateful for your mentorship, support, patience, and advice during my PhD studies. I am forever thankful!

I appreciate **Dr. Daisuke Kawashima** for his guidance and advice during my studies.

I also want to thank **Dr. Martin Wekesa Sifuna** for extending the PhD scholarship opportunity and for his guidance in the research.

I am also thankful to **Dr. Kenji Hikosaka** who provided *Plasmodium falciparum in vitro* cultures and permitted us to carry out EIS measurement experiments in his laboratory.

To **Dr. Hirokazu Sakamoto** thank you for your support during the experiments.

I also thank **Xiaoxia X Lin,** a PhD student in Dr. Hikosaka's lab for her support in culturing *Plasmodium falciparum* parasites.

To all Takei laboratory members, thank you for sharing my PhD journey and for all your support.

To everyone else who contributed to the success of this study, I say a big thank you!